University of Maribor
Faculty of Energy Technology

Journal of ENERGY TECHNOLOGY

Volume 14 / Issue 4
DECEMBER 2021
www.fe.um.si/en/jet.html

Journal of ENERGY TECHNOLOGY

VOLUME 14 / Issue 4

Revija Journal of Energy Technology (JET) je indeksirana v bazah INSPEC© in Proquest's Technology Research Database.

The Journal of Energy Technology (JET) is indexed and abstracted in database INSPEC© and Proquest's Technology Research Database.

JOURNAL OF ENERGY TECHNOLOGY

Tehnični urednik / TECHNICAL EDITOR

Sonja Novak

Tehnična podpora / TECHNICAL SUPPORT

Tamara BREČKO BOGOVČIČ

Izhajanje revije / PUBLISHING

Revija izhaja štirikrat letno v nakladi 100 izvodov. Članki so dostopni na spletni strani revije - www.fe.um.si/si/jet.html / The journal is published four times a year. Articles are available at the journal's home page - www.fe.um.si/en/jet.html.
Cena posameznega izvoda revije (brez DDV) / Price per issue (VAT not included in price): 50,00 EUR
Informacije o naročninah / Subscription information: http://www.fe.um.si/en/jet/subscriptions.html

Lektoriranje / LANGUAGE EDITING

TAIA INT d.o.o.

Oblikovanje in tisk / DESIGN AND PRINT

Foto Colarič, Boštjan Colarič s.p.

Naslovna fotografija / COVER PHOTOGRAPH

Jurij AVSEC

Oblikovanje znaka revije / JOURNAL AND LOGO DESIGN

Andrej PREDIN

Ustanovni urednik / FOUNDING EDITOR

Andrej PREDIN

Izdajanje revije JET finančno podpira Javna agencija za raziskovalno dejavnost Republike Slovenije iz sredstev državnega proračuna iz naslova razpisa za sofinanciranje domačih znanstvenih periodičnih publikacij / The Journal of Energy Technology is co-financed by the Slovenian Research Agency.

Spoštovani bralci revije Journal of energy technology (JET)

V mnogih poklicih se odpira vprašanje o njihovi prihodnosti. Odpirajo se novi poklici, nekateri stari pa žal postajajo manj aktualni. Človeštvo bo razen proizvodnje hrane in zdravja zagotovo tudi v naslednjih stoletjih in tisočletjih potrebovalo energijo. Pravzaprav človek kljub učinkoviti rabi energije potrebuje za svoj obstoj vse več energije. Zato se za prihodnost poklica energetika ne bojim, prav nasprotno, analize kažejo, da v svetu potrebujemo vse več strokovnjakov s področja energetike. Tudi v Sloveniji se v zadnjem času načrtujejo nove velike energetske investicije, kjer bi se potem lahko zaposlilo veliko energetikov. Tudi razvoj tako imenovanih zelenih tehnologij bo omogočal dodatne zaposlitve energetikov. Študij energetike seveda razen poglobljenega teoretičnega poučevanja zahteva tudi sodobne laboratorijske prostore za kakovostno opravljanje laboratorijskih vaj, diplomskih nalog, študentskih projektov... Fakulteta za energetiko ima sodobne in vrhunsko opremljene laboratorije. Da bi predstavila dosežke poglobljenega raziskovanja na področju energetike in medsebojne izmenjave mnenj, bo Fakulteta za energetiko v mesecu juniju organizirala peto mednarodno konferenco EnRe (Enegy and responsibility).

Jurij AVSEC
odgovorni urednik revije JET

Dear Readers of the Journal of Energy Technology (JET)

For many professions, the question of what awaits them is ever-present. New professions are opening up and some old ones are unfortunately becoming less relevant. In addition to food and health production, humanity will certainly need more sources of energy in the coming centuries and millennia. In fact, despite the growing efficiency with regards to energy usage, humankind needs more and more energy for its existence. For this reason, I am not afraid for the future of the energy profession; on the contrary, analysis shows that we need more and more energy experts in the world. Big new energy investments have also been planned in Slovenia recently, creating potential employment opportunities for many energy workers once construction is complete. The development of so-called green technologies will also allow for additional employment in energy companies. Of course, in addition to in-depth theoretical teaching, the study of energy also requires modern laboratory facilities for quality laboratory work, diploma theses, student projects, etc. The Faculty of Energy Technology, for one, boasts modern, state-of-the-art laboratories. In order to present the achievements of in-depth research in the field of energy, and to encourage the mutual exchange of views, the Faculty of Energy will organise the fifth international EnRe (Energy and responsibility) conference in June.

Jurij AVSEC
Editor-in-chief of JET

Table of Contents / Kazalo

Journal of Energy Technology

JET Volume 14 (2021) p.p. 11-19
Issue 4, December 2021
Type of article 1.01
www.fe.um.si/en/jet.html

EXPERIMENTAL VERIFICATION OF THE NUMERICALLY DETERMINED PARAMETERS FOR THE NON-LINEAR TWO-AXIS MODEL OF A SYNCHRONOUS MOTOR WITH INTERIOR PERMANENT MAGNETS

EKSPERIMENTALNO PREVERJANJE NUMERIČNO DOLOČENIH PARAMETROV ZA NELINEARNI DVOOSNI MODEL SINHRONSKEGA MOTORJA Z NOTRANJIMI TRAJNIMI MAGNETI

Željko Hederić[✉], Venco Ćorluka[1], Toni Varga[1]

Keywords: synchronous motor, flux linkage, interior permanent magnets, non-linear

Abstract

Synchronous machines belong to the family of electrical machines characterised by a synchronous magnetic rotating field in the air gap of the machine, the speed of which depends on the frequency of the currents in the armature winding. The paper presents procedures and methods for the numerical determination and experimental verification of the parameters for a nonlinear two-axis model of a synchronous motor with permanent magnets in the rotor (IPMSM) and a concentrated stator winding. To calculate the distribution of electro-magnetic fields in the motor accurately, models with

[✉] Prof.Dr.Sc. Željko Hederić,PhD, Faculty of Electrical Engineering, Computer Science and Information Technology Osijek, Kneza Trpimira 2B, HR-31000 Osijek, Croatia, +385 31 224 600, zeljko.hederic@ferit.hr

[1] University of Osijek, Faculty of Electrical Engineering, Computer Science and Information Technology Osijek, Kneza Trpimira 2B, HR-31000 Osijek, Croatia

distributed parameters are used in motor design, for which the Finite Element Method (FEM) is usually employed. The improvement by using the model with concentrated parameters considerably simplifies the physical model, by describing it with a system of (non)linear differential equations, the so-called partial differential equations, which is presented in this paper.

Povzetek

Sinhronski stroji spadajo v družino električnih strojev, za katere je značilno sinhrono magnetno vrtljivo polje v zračni reži stroja, katerega hitrost je odvisna od frekvence tokov navitja armature. V prispevku so predstavljeni postopki in metode za numerično določanje in eksperimentalno preverjanje parametrov za nelinearni dvoosni model sinhronskega motorja s trajnimi magneti v rotorju (IPMSM) in koncentriranim statorskim navitjem. Pri načrtovanju motorjev se za natančnejši izračun porazdelitve elektromagnetnih polj v motorju uporabljajo modeli s porazdeljenimi parametri, za kar se običajno uporablja metoda končnih elementov (MKE). V prispevku je predstavljena izboljšava, ki z uporabo modela s koncentriranimi parametri v osnovi znatno poenostavi fizični model, tako da ga opiše s sistemom (ne)linearnih diferencialnih enačb, tako imenovanih delnih diferencialnih enačb.

1 INTRODUCTION

A synchronous motor with interior permanent magnets and concentrated winding (IPMSM) has 12 stator slots and 10 magnetic poles inside the rotor. The motor has an uneven air gap. The mathematical modelling starts with setting up the voltage equations for each winding in a three-phase system [1, 2]:

$$u_{\mathrm{abc}} = Ri_{\mathrm{abc}} + \frac{\mathrm{d}}{\mathrm{d}t}\Psi_{\mathrm{abc}} + \frac{\mathrm{d}}{\mathrm{d}t}\Psi_{\mathrm{mabc}} \tag{1.1}$$

The contributions of a flux linkage from a permanent magnet are represented by Ψ_{mabc} in a three-phase system of motor supply. By converting a three-phase time system into a two-axis position system, one obtains the voltage equation for a magnetically nonlinear dynamic model of a synchronous motor with permanent magnets in a d-q system:

$$\begin{bmatrix} u_d \\ u_q \end{bmatrix} = R\begin{bmatrix} i_{\mathrm{d}} \\ i_q \end{bmatrix} + \boldsymbol{M}_1 \cdot \frac{\mathrm{d}}{\mathrm{d}t}\begin{bmatrix} i_d \\ i_{\mathrm{q}} \end{bmatrix} + \frac{\mathrm{d}\theta}{\mathrm{d}t} \cdot \boldsymbol{M}_2 \tag{1.2}$$

where $\boldsymbol{M}_1$ and $\boldsymbol{M}_2$ are the system matrices:

$$\boldsymbol{M}_1 = \begin{bmatrix} \frac{\partial \psi_\mathrm{d}}{\partial i_\mathrm{d}} & \frac{\partial \psi_\mathrm{d}}{\partial i_\mathrm{q}} \\ \frac{\partial \psi_\mathrm{q}}{\partial i_\mathrm{d}} & \frac{\partial \psi_\mathrm{q}}{\partial i_\mathrm{q}} \end{bmatrix} \tag{1.3}$$

$$\mathbf{M}_2 = \begin{bmatrix} \frac{\partial \psi_\mathrm{d}}{\partial \theta} \\ \frac{\partial \psi_\mathrm{q}}{\partial \theta} \end{bmatrix} + \begin{bmatrix} -\psi_\mathrm{q} \\ \psi_\mathrm{d} \end{bmatrix} + \begin{bmatrix} \frac{\partial \psi_\mathrm{md}}{\partial \theta} \\ \frac{\partial \psi_\mathrm{mq}}{\partial \theta} \end{bmatrix} + \begin{bmatrix} -\psi_\mathrm{mq} \\ \psi_\mathrm{md} \end{bmatrix} \tag{1.4}$$

The partial derivatives within the matrices, as well as the flux linkage of the stator ($\Psi_\mathrm{d}, \Psi_\mathrm{q}$) and the flux linkage of the permanent magnets (Ψ_mq, Ψ_md), represent the parameters of the model which must be determined experimentally due to their nonlinearity. The magnetic fluxes of the stator depend on the currents and position of the rotor, while the magnetic fluxes of the permanent magnet depend only on the position of the rotor.

2 DETERMENING NONLINEAR PARAMETERS BY THE FINITE ELEMENT METHOD

The magnetic nonlinear parameters required for the flux linkages and their partial derivatives can be determined with the Finite Element Method (FEM) (or the distributed parameter model), or experimentally. The input variables are the stator current parameters i_d, i_q and the rotor position θ. Flux linkages are obtained by solving the Poisson's equation via the vector of magnetic potential [2, 3]:

$$\frac{\partial^2 \boldsymbol{A}}{\partial x^2} + \frac{\partial^2 \boldsymbol{A}}{\partial y^2} = -\mu \boldsymbol{J} \tag{2.1}$$

The relation between the magnetic flux and the vector of the magnetic potential according to Stokes' theorem is:

$$\Phi^e = \oint_C \boldsymbol{A}^e \mathrm{d}\boldsymbol{l}^e \tag{2.2}$$

The magnetic flux Φ_s for one winding is equal to the difference between the magnetic potential of the left and right sides of the winding and the product of the winding length:

$$\Phi_s = (\boldsymbol{A}_{ls} - \boldsymbol{A}_{2s}) \cdot l_{Fe} \tag{2.3}$$

Multiplying the magnetic flux by a total number of windings gives a flux linkage Ψ:

$$\Psi = \mathrm{N} \cdot \Phi \tag{2.4}$$

After the FEM calculation on the IPMSM is completed, obtained three-phase values are transformed back into a two-axis coordinate system, by the inverse transformation matrix. The result of numerical and experimental determination are flux linkages Ψ_d and Ψ_q as functions of currents i_d, i_q and rotor position θ.

The current and position dependent flux linkages, which represent the parameters of the dynamic model, can be solved by a model with distributed parameters using FEM. Numerical calculation with FEM is carried out in a real coordinate system for IPMSM, i.e. in a three-phase system. In the calculation of FEM, the values of three-phase currents must be inserted, which, in turn, are solved by the currents of the two-axis model with two-phase to three-phase transformation. To calculate the three-phase input alternating currents for the numerical algorithm, transformation matrices must be used, with which it is possible to change from a two-axis position system to a three-phase time system, and vice versa.

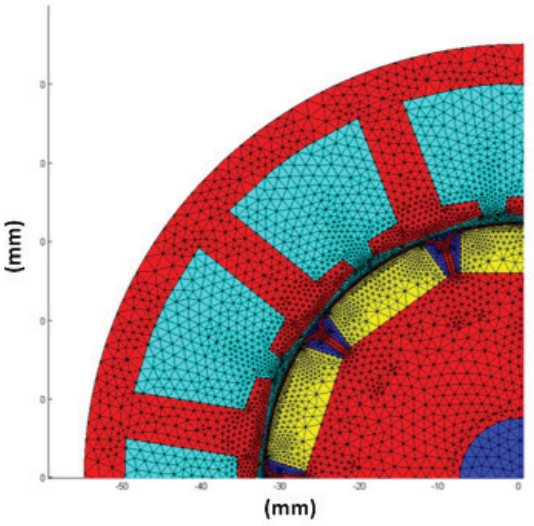

Figure 1: *Discretisation of space on finite elements*

The condition for the correct use of transformation matrices is that the magnetic conditions do not change during the transformation [2,4,5].

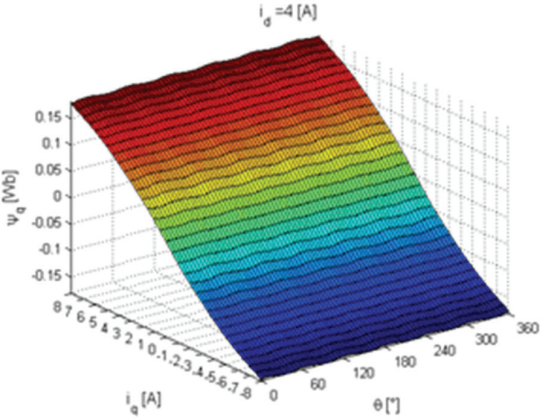

Figure 2: *Graphic representation of the magnetic flux linkage distribution Ψ_q for current i_d = 4 A*

The results of FEM calculation are flux linkages: Ψ_a (i_a, i_b, i_c, θ), Ψ_b (i_a, i_b, i_c, θ) and Ψ_c (i_a, i_b, i_c, θ). Furthermore, using a three-phase to two-axis transformation, it is necessary to convert the linked magnetic fluxes into a two-axis model Ψ_d (i_d, i_q, θ) and Ψq (i_d, i_q, θ) used in a magnetically nonlinear dynamic model. The magnetic nonlinear properties to be determined can be divided into two groups. The first group includes flux linkages that result from the excitation of permanent magnets. These flux linkages are current independent. The second group are flux linkages resulting from stator currents.

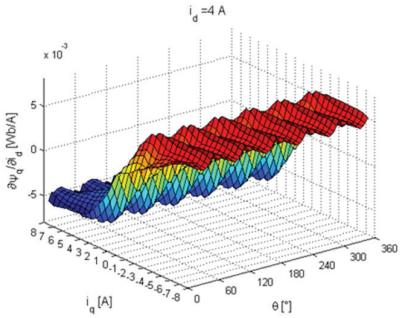

Figure 3: *Graphic representation of the distribution of partial derivation* $\partial \Psi_q / \partial i_d$ *for current id = 4 A*

The numerical calculations of FEM for the flux linkages were done by discretisation of the motor through 38 616 derivations in the form of a three-dimensional graph.

3 EXPERIMENTAL DETERMINATION OF FLUX LINKAGES CAUSED BY STATOR CURRENTS

The parameters of a dynamic model of a synchronous motor can be determined experimentally, because the flux linkages in the d-axis Ψ_d (i_d, i_q, θ) and in the q-axis Ψ_q (i_q, i_d, θ) depend on the currents and the rotor position, while the flux linkages of permanent magnets Ψ_{mdq} (θ) depend only on the rotor position. The flux linkages (Ψ_d and Ψ_q) in d and q-axes are determined by an experiment with a locked rotor, whereby the position of the rotor must be known [5,6].

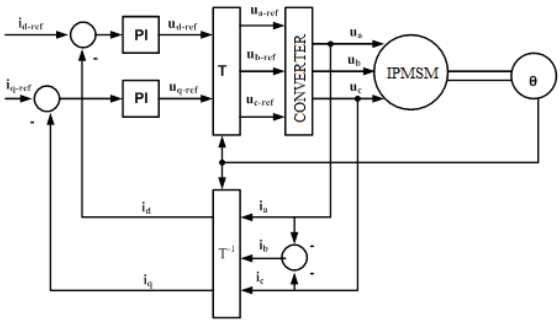

Figure 4: *Measuring system for determining current and position dependent flux linkages*

The procedure is carried out by applying a rectangular variable voltage in one axis and a constant current in the other axis. The measuring system for determining current and position-dependent

flux linkages flows is shown in Figure 4. The elements of the measuring system are: The tested IPMSM motor, a three-phase converter, a module with a signal processor with input and output units, a module for pulse-width modulation, a rotor position meter (MP), two measuring converters for current measurement. Current control is performed via PI regulators. [7,8]
The voltage converter applies the constant current i_q in the q-axis, and the variable rectangular voltage u_d of a certain period in the d-axis. The duration of this period is determined as the time during which the current assumes a constant value in the greater part of the half-period.

In further examples, flux linkages are determined with given current values. As the rotor is locked, all members in the voltage equation with change in the angle dθ are dropped, so the equation takes the form [9]:

$$u_{\mathrm{d}} = i_{\mathrm{d}} R_{\mathrm{d}} + \frac{\mathrm{d}\,\psi_{\mathrm{d}}}{\mathrm{d}t} \tag{3.1}$$

For the calculation of the flux linkage ψ_{d} numerical integration must be applied:

$$\psi_{\mathrm{d}}(t) = \int_0^t \left(u_{\mathrm{d}}(\tau) - R i_{\mathrm{d}}(\tau)\right) d\tau \tag{3.2}$$

According to this expression, flux linkages Ψ_{d} and Ψ_{q} are calculated for i_q=7 A, i_d=0, at time period T = 0.4 s with numerical integration to be compared with the experimentally obtained values.

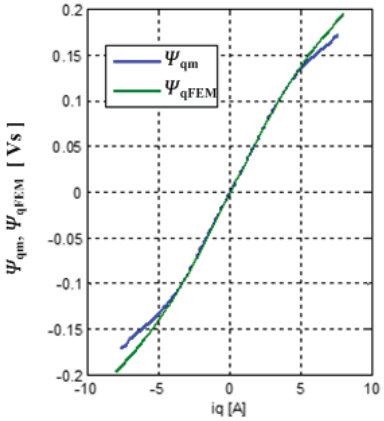

Figure 5: *Comparison of the measured Ψ_{qm} and numerically calculated Ψ_{qFEM} as a function of current i_q*

A comparison of the measured results with the values obtained by the FEM calculation can be seen in Fig. 5, and only small deviations are observed. The deviations can be explained with the error of the numerical calculation, as well as the non-uniform voltages and currents applied to the stator winding from the frequency converter. Given the curve dependencies of flux linkages are about current values (in this case the values are currents from -8 A to 8 A, with a step of 0.5A) they can provide the uniform (i) characteristic at characteristic current values. From the uniform characteristics thus obtained, two two-dimensional matrices can be formed: Current and position-dependent magnetic fluxes Ψ_d (i_d, i_q, θ) and Ψ_q (i_q, i_d, θ).

4 EXPERIMENTAL DETERMINATION OF THE PERMANENT MAGNET FLUX LINKAGES

The measurement of the induced voltage on the stator windings is carried out at a constant rotor speed. The measuring system for determining the flux linkage of permanent magnets, shown in Figure 6, consists of a DM drive machine controlled by a measuring transducer. The DM drive machine is connected mechanically to the tested IPMSM motor by an axle on which the MP rotor position transducer is also installed. The induced voltages in all three phases of the tested motor are measured by a voltage converter VC and stored in a PC via the A/D card as a rotor position data. In this case, the stator currents in d-axis and q-axis are equal to zero, and only the flux linkages of the permanent magnets in d-axis and q-axis and the angular velocity remain [5].

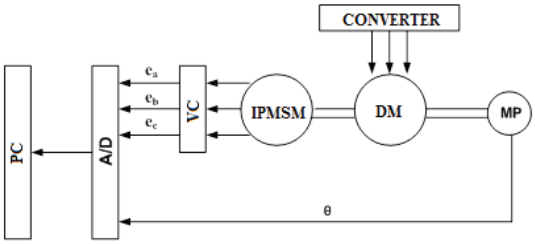

Figure 6: *Measurement system for determining the flux linkages of permanent magnets*

For the open terminals on the stator, the voltage equations have the form:

$$e_{\mathrm{d}} = -\psi_{\mathrm{mq}} \frac{\mathrm{d}\theta}{\mathrm{d}t} + \frac{\partial \psi_{\mathrm{md}}}{\partial \Theta} \frac{\mathrm{d}\theta}{\mathrm{d}t} \tag{4.1}$$

$$e_{\mathrm{q}} = \psi_{\mathrm{md}} \frac{\mathrm{d}\theta}{\mathrm{d}t} + \frac{\partial \psi_{\mathrm{mq}}}{\partial \Theta} \frac{\mathrm{d}\theta}{\mathrm{d}t} \tag{4.2}$$

After sorting, a second-order partial differential equations for Ψ_{md} and Ψ_{mq} are obtained:

$$\psi_{\mathrm{md}} + \frac{\partial^2 \psi_{\mathrm{md}}}{\partial \theta^2} = \frac{\partial}{\partial \theta}\left(\frac{e_{\mathrm{d}}}{\omega}\right) + \frac{e_{\mathrm{q}}}{\omega} \tag{4.3}$$

$$\psi_{\mathrm{mq}} + \frac{\partial^2 \psi_{\mathrm{mq}}}{\partial \theta^2} = \frac{\partial}{\partial \theta}\left(\frac{e_{\mathrm{q}}}{\omega}\right) - \frac{e_{\mathrm{d}}}{\omega} \tag{4.4}$$

The numerical solution of these equations for the measured values of induced voltages and the given frequency, gives the values of the flux linkages of the permanent magnets, depending on the position of the rotor. An example of the calculation of the flux linkage of permanent magnets is carried out in such a way that the rotor rotates at a constant rated speed, and the three-phase induced voltages e_a, e_b and e_c are recorded on open stator terminals which are transformed into a two-axis d-q system e_d and e_q. [10-12]

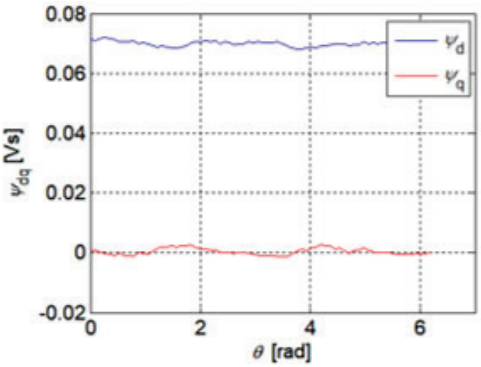

Figure 7: *Flux linkages in the d-q axis obtained by the measurement*

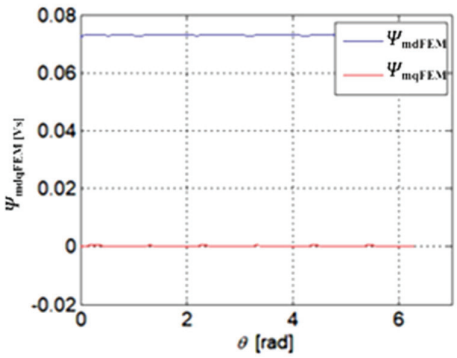

Figure 8: *Flux linkages in d-q axis obtained by the FEM calculation*

Solution of the system of equations (Eq. 4.1 - Eq. 4.4) for the flux linkages of the permanent magnet Ψ_{md} and Ψ_{mq} is shown in Fig. 7, while solution using the FEM calculation is shown in Fig. 8.

3 CONCLUSION

The problem of creating a magnetic nonlinear model and incorporating the results of the FEM calculations (distributed parameters) was solved by analysing all the subsystems (electrical and mechanical) that are connected nonlinearly.

The paper explains an algorithm for the correct definition of the model using partial differential equations, i.e. the calculation of the partial derivatives of the flux linkages. The magnetically nonlinear dynamic model of IPMSM is useless as long as the magnetically nonlinear properties and their partial derivatives are undetermined.

These magnetically nonlinear characteristics represent the variable parameters of the derived model and are determined by the Finite Element Method (FEM). To verify the model, i.e. the numerical calculations of the FEM, a measuring system was prepared and experimental testing was performed on the sample IPMSM.

References

[1] **Jacek F. Gieras**, "Permanent magnet motor technology: design and applications", CRC Press, 2010.

[2] **T. Marčić, G. Štumberger, B. Štumberger, M. Hadžiselimović and P. Virtič,** *"Determining Parameters of a Line-Start Interior Permanent Magnet Synchronous Motor Model by the Differential Evolution",* in IEEE Transactions on Magnetics, vol. 44, no. 11, pp. 4385-4388, Nov. 2008

[3] **C. C. Hwang, S. P. Cheng, and C. M. Chang,** "*Design of High-Performance Spindle Motors With Concentrated Windings",* IEEE Transactions On Magnetics, Vol. 41, No. 2, February 2005.

[4] **G. H. Kang, J. P. Hong, G. T. Kim, and J. W. Park,** *"Improved parameter modeling of interior permanent magnet synchronous motor based on finite element analysis"*, IEEE Trans. Magn., vol. 36, pp. 1867-1870, July 2000.

[5] **Z. Xinghua and C. Pengfei,** *"Efficiency optimization of a direct torque controlled interior permanent magnet synchronous motor considering iron losses", 2016 19th International Conference on Electrical Machines and Systems (ICEMS)*, 2016, pp. 1-5.

[6] **S. P. Lim and K. J. Tseng**, "*Dynamic model of an interior permanent magnet motor with skewed stator slots*," IECON'99. Conference Proceedings. 25th Annual Conference of the IEEE Industrial Electronics Society (Cat. No.99CH37029), 1999, pp. 1471-1476 vol.3

[7] **M. HadžiselimoviĆ, G. Štumberger, B. Štumberger and I. Zagradišnik**, "*Magnetically nonlinear dynamic model of a synchronous motor with permanent magnets",* J. Magn. Magn. Mater., vol. 316, pp. e257-e260, 2007.

[8] **A. Khlaief, M. Bendjedia, M. Boussak and M. Gossa**, "*A nonlinear observer for high-performance sensorless speed control of IPMSM drive"*, IEEE Trans. Power Electron., vol. 27, no. 6, pp. 3028-3040, Jun. 2012

[9] **N. Yang, G. Luo, W. Liu and K. Wang**, "*Interior permanent magnet synchronous motor control for an electric vehicle using a look-up table"*, Proceedings of The 7th International Power Electronics and Motion Control Conference, 2012, pp. 1015-1019

[10] **S. P. Lim and K. J. Tseng**, "*Dynamic model of an interior permanent magnet motor with skewed stator slots*", IECON'99. Conference Proceedings. 25th Annual Conference of the IEEE Industrial Electronics Society (Cat. No.99CH37029), 1999, pp. 1471-1476 vol.3

[11] **X. Xiao, C. Chen and M. Zhang**, "Dynamic Permanent Magnet Flux Estimation of Permanent Magnet Synchronous Machines", in IEEE Transactions on Applied Superconductivity, vol. 20, no. 3, pp. 1085-1088, June 2010

[12] **E. Sokolov and M. Mihov**, "*Parameter Estimation of an Interior Permanent Magnet Synchronous Motor*", 2019 16th Conference on Electrical Machines, Drives and Power Systems (ELMA), 2019, pp. 1-5

JET Journal of Energy Technology

JET Volume 14 (2021) p.p. 21-39
Issue 4, December 2021
Type of article 1.01
www.fe.um.si/en/jet.html

HRSG SYSTEM DESCRIPTION AND WATER-STEAM ANALYSIS AT THE HRSG COLD START-UP

OPIS SISTEMA HRSG IN ANALIZA VODE-PARE PRI HLADNEM ZAGONU

Dušan Strušnik[1]*

Keywords: boiler, duct, flue gas, heat recovery, stack, steam generator, superheater

Abstract

The basic purpose of this paper is to present the HRSG system description in detail and possibility analysis of preventing the HRSH water-steam generated release into the atmosphere through the sky valves during the HRSG cold start-up. The steam released into the atmosphere by the cross sky valve is not an adequate solution for the following reasons: Noise prevention, water losses, thermal heat release into the environment, etc. In this paper, the possibilities and solutions are investigated in order to avoid the HRSG start-up sky venting. For this purpose, the steam quality data at HRSG cold start-up is analysed, and the possibility is examined of discharging the HRSG generated steam at the start-up via a new start-up pipeline into the existing dump condenser, or into the start-up flash tank or into the blowdown tank. The results show that, at the first 3 minutes of cold start-up, the HRSG generated only water, and this water should not be discharged into the HP or IP pipeline headers. The HRSG generates a mixture of water and steam only after 4 minutes from the start-up. For that reason it is not recommended to drain the water-steam mixture at the HRSG start-up into the new start-up pipeline, but it is recommended to drain the water and steam mixture formed during the HRSG start-up into the new start-up flash tank, or into the blowdown tank. The flash tank, and also the blowdown tank, should be appropriately dimensioned.

* Corresponding author: Dušan Strušnik, Energetika Ljubljana d.o.o., TE-TOL unit, Toplarniška 19, Ljubljana, E-mail address: dusan.strusnik@gmail.com

[1] Energetika Ljubljana d.o.o., TE-TOL unit, Toplarniška 19, Ljubljana

Povzetek

Osnovni namen prispevka je podrobna predstavitev HRSG-ja in analiza možnosti zmanjšanja izpusta generirane pare v atmosfero ob hladnem zagonu. Izpust zagonske pare v atmosfero ni najboljša možna rešitev, saj se s tem poveča zvočna obremenitev okolja, odvod kotlovske vode in toplotne energije v okolje itd. V tem prispevku so analizirane možne rešitve preprečitve odvoda zagonske pare v atmosfero, tako da se mešanica vode-pare ob hladnem zagonu HRSG-ja odvede v novi zagonski parovod, separatorsko posodo ali v posodo za odvodnjavanje. Analizirani pa so bili tudi podatki kvalitete pare ob zagonu HRSG-ja. Rezultati pokažejo, da prve 3 minute HRSG generira samo vodo, ki pa se ne sme odvesti v HP oziroma IP zbiralno kom parovoda. Šele po 4 minutah HRSG prične generirati mešanico vode-pare. Zato se pri hladnem zagonu ne priporoča odvod generirane pare v novi zagonski parovod, ampak da se navedena mešanica vode-pare, ki nastane pri hladnem zagonu HRSG-ja, odvede v separatorsko posodo oziroma v posodo za odvodnjavanje. Navedeni posodi morata biti temu primerno dimenzionirani.

1 INTRODUCTION

The electricity production using a gas turbine and an electric generator can be provided in an open cycle plant, where the hot flue gases from the gas turbine are released through the stack directly into the atmosphere. The disadvantage of this process is the relatively low efficiency of the open cycle plant, which, in practice, ranges from 30% to 40%. If the open cycle is upgraded with a Heat Recovery Steam Generator (HRSG) and with the steam turbine, the realistically achieved efficiencies of this process range up to 85%. Such a process is called a combined cycle gas turbine. The operation of this type of combined cycle gas turbine in energy systems is called a combined heat and power plant.

The purpose of the HRSG is to recover the maximum of the remaining energy contained in the flue gas at the outlet of the gas turbine. The recovered heat is transferred to feedwater in order to produce steam at the 2 different pressure levels required by the steam turbine. The HRSG feeds a steam turbine. The gas turbines are fired with natural gas as the main fuel and light fuel oil as a back-up fuel. There is no bypass stack. Therefore, the boiler runs in line with the gas turbine. The HRSG scope includes heat exchangers, a boiler casing, boiler inlet and outlet ducts, district heating recirculation pumps, a flash tank, a blowdown tank, boiler drums, piping, valves, instrumentation and air distribution, and nitrogen distribution. The most important components of an HRSG are shown in Figure 1. The HRSG is of the vertical boiler type with natural circulation; the exhaust gases have an upward path while crossing the different exchangers. The heat exchangers are made of finned tubes installed horizontally, with return bends, between an inlet and an outlet header. They are shop-assembled in 5 modules: 5 modules on the height and 1 module on the width of the HRSG. Each exchanger is inserted into the vertical gas flow. A casing is constructed around them to form a sealed unit. The casing is manufactured from steel sheets, without any refractory concrete or water tubes panel, and is insulated internally on the whole HRSG from the inlet duct to the stack. All exchangers are hung on horizontal hot beams, which are supported by the main boiler steel structure. The casing is also supported by the steel structure. This design allows free expansion, downward and laterally. The HRSG stack is supported by the steel structure penthouse. The natural circulation principle is used within the boiler evaporator drum loops, high pressure (HP), and intermediate pressure (IP) through the thermosyphon effect. Two pressure levels are installed in the HRSG: The two circuits produce the steam flows at two different required pressures and temperatures.

The work done thus far in the above-mentioned area is based on an optimal synthesis and design of the HRSG, for which Manassaldi et al. [1] presented the HRSG mathematical programming. Ahmed et al. [2] carried out modelling and practical studying of the HRSG drum dynamics and approached the point effect on the control valves. Wang et al. [3] conducted an experiment and optimisation analysis of a new kind of once-through heat HRSG based on exergy and economy. Using the calculation method, Naserabad et al. [4] optimised HRSG configurations on the steam power plant`s repowering specifications. Moreover, Beaujardiere et al. [5], Mokhtari et al. [6] and Zebian [7] analysed HRSG operational performance. However, we have not yet identified an HRSG system description in detail in the available literature .

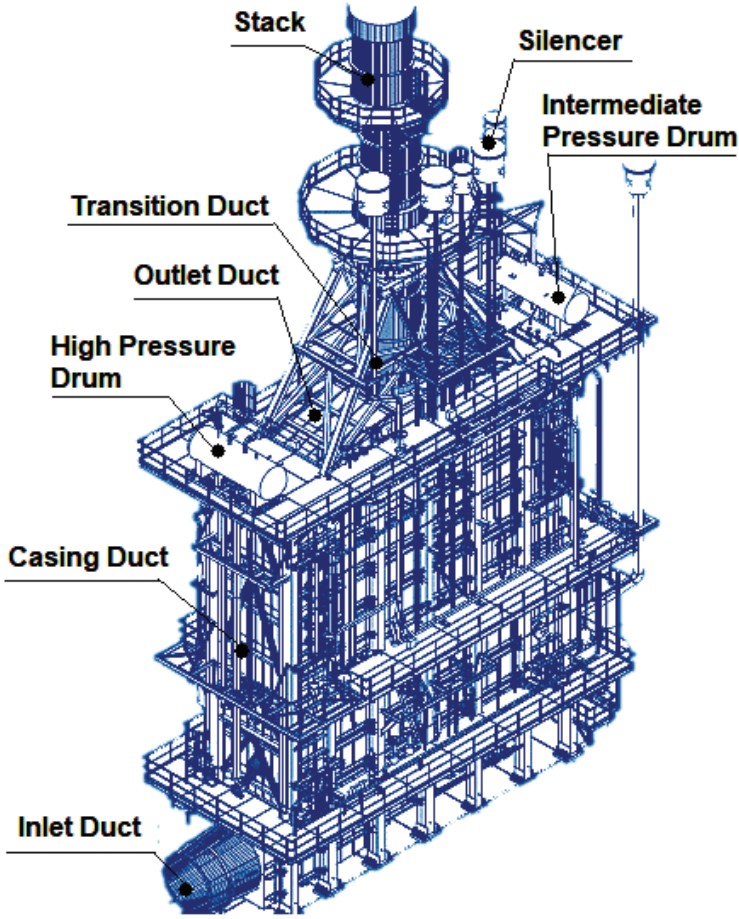

Figure 1: *The most important components of an HRSG [8]*

A district heating system is installed to heat water coming from a district heating system and going to a district heating system. The district heater is recirculated with hot water in order to reach at its inlet at a minimum temperature above the acid dew point and a margin. This value is representative of the temperature at which sulphur may deposit on the tubes (flue gas acid, dew point temperature), and it is of prime importance to make sure that such a minimum water

temperature (which depends on the sulphur content in the fuel) be matched, so as to avoid corrosion. A bypass line allows partial or complete bypassing of the district heater in order to control the final temperature of the water going to the DH system. The HP steam temperatures are controlled by water injection (through attemperators located on the HP superheaters line), ensuring adequate steam turbine inlet temperatures.

The structure of the paper is composed in such a way that the system description of the HRSG individual components, such as the HRSG pressure parts, HRSG non-pressure parts and steel structure are presented first. Then the system description of the auxiliary equipment is presented and the water-steam analysis at the HRSG cold start-up is carried out at the end.

2 SYSTEM DESCRIPTION

2.1 Pressure parts, description of the heat exchangers

Each heat exchanger is made up of horizontal finned tubes connected to each other by means of bare tube bends. The finned tubes are staggered in the tube bank. The fins are made of spiral steel strips. They are welded in a continuous way on the bare tubes. These fins are serrated. The tube quantity in a heat exchanger and the number of fins per metre are calculated in accordance with the required surface given by the heat balance of the boiler. The number of tubes in parallel depends on the water or steam flow. The fluid velocity in the tubes is selected according to the manufacturer`s experience. Appropriate material has been selected to avoid flow-assisted corrosion. The tube arrangement the width and length of the exchangers - is optimised in accordance with the gas velocity, the pressure drop, the water and steam pressure drop through the circuits and the shipment facilities. Each tube is simply supported on the tube sheets to allow free thermal expansion of the tubes. The touch points between tubes and tube sheets are the spiral fins: Wearing of the tubes themselves is, therefore, avoided. The heat exchanger modules are hung from the hot beams by means of prefabricated hangers. The HRSG cross-section with the 5 modules of heat exchangers is shown in Figure 2.

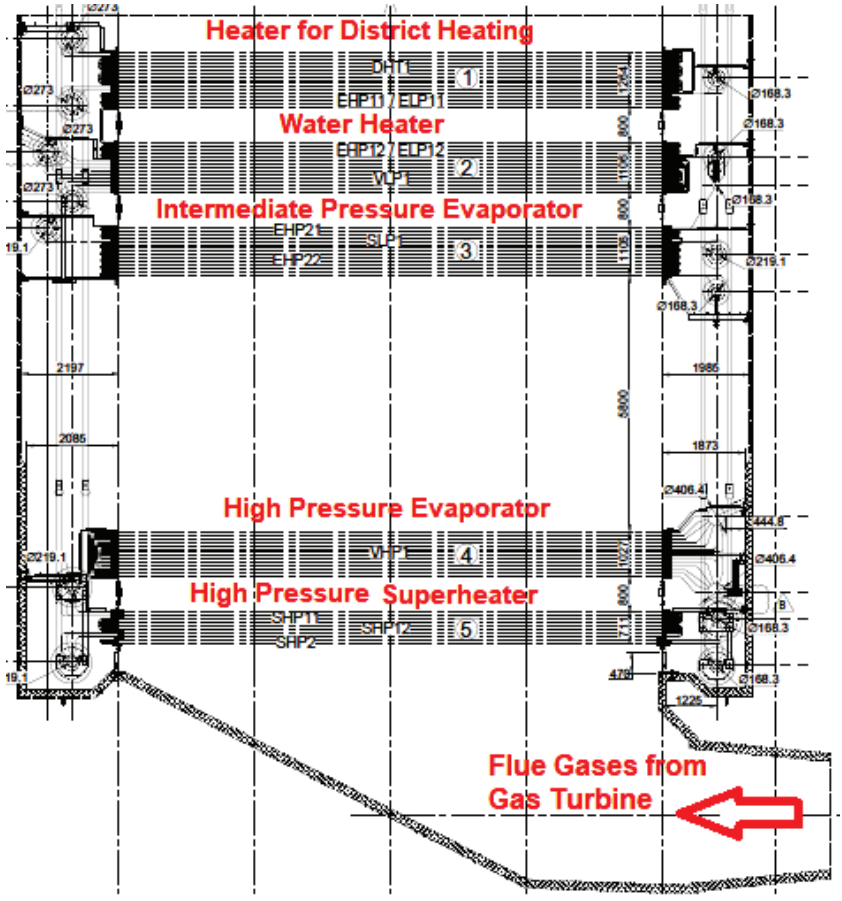

Figure 2: *The HRSG cross-section with the 5 modules of heat exchangers [8]*

The heat exchanger headers are enclosed in a box formed by the gas-tight boiler casing faces, the tube baffles and the closing plates, to avoid internal gas by-pass. The headers are provided with borescope holes in order to allow internal examination of each header. The heat exchangers are grouped in different sections to form an HP circuit, an IP circuit and a district heater circuit. In order to produce steam, the circuits comprise economisers, evaporators and superheaters. The functions of these heat exchangers are as follows:

- The economiser recovers the remaining heat contained in the flue gas at the evaporator outlet in order to heat up the water flow.
- The evaporator generates steam through a circulation loop to and from the HRSG drum.
- The superheater permits the saturated steam heating from the drum temperature up to the required value.
- The district heater circuit produces hot water for the district heating system by heating up the cold water coming from the district heating system. The water coming from the outlet of the district heater is recirculated in the district heater to increase the temperature at its inlet (the temperature depends on the actual sulphur content of the burnt gas in the gas turbine).

2.2 Pressure parts, natural circulation

The natural circulation through the HP / IP evaporators is ensured by the density difference between the water coming from the drum to the evaporator inlet header and the two-phase water/steam mixture between the outlet header and the return to the drum, as well as the transition phase that happens in the whole exchanger. During start-up, water flows naturally through the evaporator when the first bubbles of steam are generated. Natural circulation through the HRSG drum is shown in Figure 3.

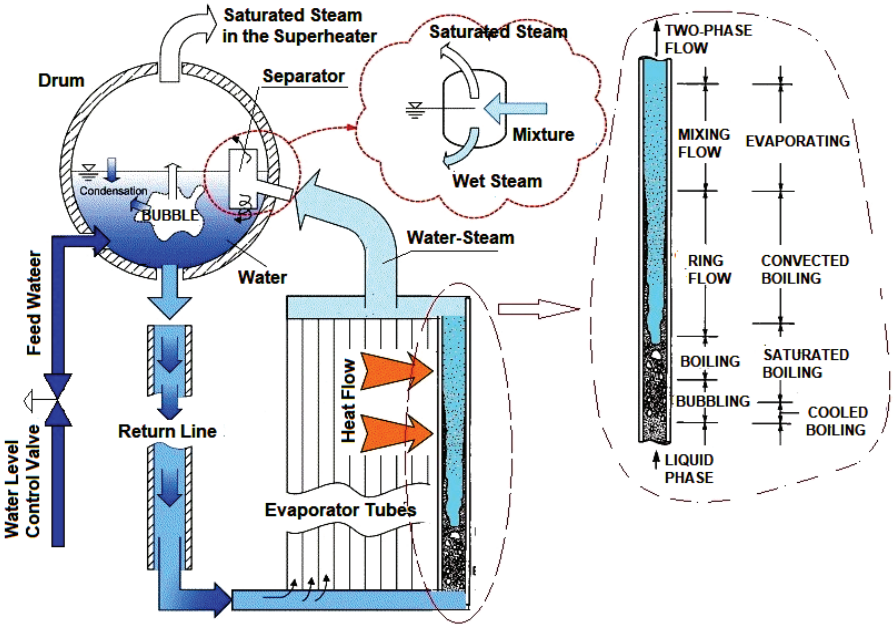

Figure 3: *Natural circulation through the HRSG drum*

2.3 Pressure parts, boiler drum description

The purposes of the boiler drums are multiple:

- To ensure a good mixing of the feedwater and boiler water;
- To constitute a water reserve in case of a feedwater pump trip (run-out-time);
- To allow water/steam expansion mainly during start-up, when the first steam produced in the evaporator sends back to the drum the water contained in the evaporator tubes (swelling effect), and
- To ensure the water and steam separation.

The steam and water separation is achieved by means of a mesh type separator installed in the upper part of the drum. The steam drums are equipped with all the required devices for their function:

- Mesh steam dryers;
- Steam distribution header;
- Water outlet (down comer) to the evaporator with an anti-vortex;

- Steam inlet nozzle from the evaporator, and
- Steam outlet nozzle to the superheater.

The HRSG drum is shown in Figure 4.

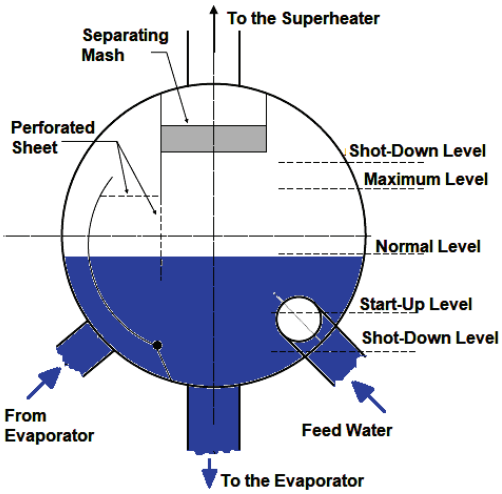

Figure 4: *The HRSG drum*

The HRSG equipment includes a manhole, nozzles for level measurement, pressure measurement, continuous and intermittent blowdown lines, nitrogen injection (on which the drum pressure gauges are connected, and skin temperature measurement for the drum. Connections between the drums and heat exchangers are realised by means of piping which is welded directly onto the drum nozzles, and, as such, all piping is free to expand without inducing any undue stress on the drum. In order to keep the drum level within the alarm limits during start-up (cold), it is necessary that the drum level is adjusted to the start-up level just above the low level. For the HP and IP circuits, the feedwater control valves are installed downstream of the economisers. Hence, the pressure inside the tubes is equal to the feedwater pump pressure, and is always higher than the pressure inside the drum (saturation pressure). Consequently, the risk of streaming is avoided.

2.4 Non-pressure parts, boiler casing

The complete heat exchangers with their headers and the tube sheets are within a gas-tight enclosure made of welded steel sheet panels, the boiler casing. Different to conventional boilers, the casing is made of steel sheets without any refractory concrete or water tube panels and is insulated internally and provided with a stainless steel liner. The casing is supported by the steel structure and is pressure resistant. Stiffeners are provided so that the enclosure can withstand the gas inner pressure. The boiler casing is equipped with access doors for internal inspection at each interblock level. The header boxes are equipped with closing plates to avoid flue gas circulation. The HRSG casing steel structure is shown in Figure 5 and the HRSG closing plates are shown in Figure 6.

Figure 5: *The HRSG casing steel structure*

Figure 6: *The HRSG closing plates*

2.5 Non-pressure parts, ductwork

The inlet ductwork and casing up to stack transition piece (outlet ductwork) are provided to convey the hot gases from the gas turbine exhaust to the boiler, then to the atmosphere. The ductwork is made of steel sheet panels internally insulated, provided with a stainless steel liner calculated to have a metal temperature of a maximum of 55°C. The inlet ductwork and casing to the stack transition up to the weather damper are insulated internally. No refractory concrete is installed in either the boiler nor in the ductwork; the thermal inertia is very low; the system allows rapid temperature changes without constraints, and the maintenance costs are minimal. As with the boiler casing, adequate stiffeners are installed on the ductwork to withstand the inner gas pressure. The whole exhaust system is designed for 0.05 design pressure. The inlet ductwork, i.e. the layout of the gas duct between the gas turbine and the boiler, is drawn in accordance with the site requirements, as indicated on the general arrangement drawing. The outlet ductwork is the boiler outlet duct, which is the transition piece between casing and stack. It has a gas exhaust function. The boiler sectional area is reduced through the outlet duct, in order to increase the gas velocity to the specified gas velocity.

2.6 Non-pressure parts, boiler stack

The HRSG main stack is a cylindrical section, and is constructed as follows: Carbon steel sheets which withstand all stresses due to the stack weight, wind and seismic loads. Outside this shell, heat insulation covers the stack. The thickness of this heat insulation is designed for personal protection, and aluminium cladding is provided to cover the heat insulation. The stack is equipped with aviation warning lights. Aircraft warning lights will conform to the Standard. The top elevation of the stack and its diameter are respectively 65 m and 2,66 m. Figure 7 shows the HRSG upper part stack lifting.

Figure 7: *The HRSG upper part stack lifting*

2.7 Non-pressure parts, inlet duct and elbow duct

The inlet duct casing and elbow duct casing are made of carbon steel material, insulated internally and covered in steel sheeting. The inlet duct panels are also insulated internally. The conception and the design of the inlet duct casing are shown in Figure 8.

Figure 8: *The HRSG inlet duct erection*

2.8 Auxiliary equipment

2.8.1 Pressure relief valves

The pressure relief valves are selected according to the codes and specifications for the material, quantity, set point and capacity. Valves are provided on the superheaters for the steam part, with a sensor line connection from the drum and on the economisers, and district heater lines for the water part. The steam pressure relief valves are controlled by a pneumatic control unit (fed by instrument air). A triple redundancy of pressure switches is present during the operation, 1 on the drum and 2 at the outlet of the superheater. All the steam pressure relief valves are welded. The steam pressure relief valves discharge to the atmosphere by means of a vertical exhaust pipe equipped with a silencer.

2.8.2 Blowdown tank

The Blowdown tank is a vertical tank whose function is to collect all drains from the boiler, and to allow the water expansion and flashing-up to the atmospheric pressure. The drains are connected to the horizontal inlet headers fitted tangentially to the tank, in order to permit the steam/water separation by centrifugation. Continuous, intermittent blowdown drains and steam drip leg drains are provided with motor operated valve control from the control system. Its shell

is fitted with an internal shield to protect it against erosion. The resulting steam is simply blown into the atmosphere by means of a vertical exhaust pipe equipped with a silencer to limit noise, and water is discharged to the HRSG plant drain system by means of an extraction pumping system. The heat-insulated blowdown tank is equipped with two level transmitters to ensure water availability for the blowdown pumps. The blowdown tank is shown in Figure 9.

Figure 9: *The Blowdown tank*

2.8.3 Weather protection damper

A weather damper is provided at the top of the HRSG, within the stack. Its function is to prevent rain from falling inside the HRSG during a stoppage, and to break the natural draught during a stoppage in order to keep the HRSG as hot as possible. This damper, made mainly from carbon steel, is equipped with an electric actuator, with all the necessary devices to prevent the damper being closed during the operation, and also with a rainwater disposal system. Furthermore, this damper is self-opening when the gas pressure reaches approximately 10 mbar. The HRSG water dumper is shown in Figure 10.

Figure 10: *The HRSG water dumper drive*

2.8.4 Attemperators

The HP circuit is equipped with one inter-stage, spray type attemperator, located in the superheater's lines. The steam pipe will have a thermal liner. When the control loop requests a steam temperature reduction, a pneumatically operated control valve opens and water is sprayed into the main steam piping to control the steam temperature within from 3 °C to 5 °C during steady state operations. The HP attemperation water is a mixture of cold and hot water extracted from the HP economiser inlet and the HP economiser outlet.

2.8.5 Sparging

During short-term outages, it is preferable to maintain the pressurised HRSG sections in order to provide freezing protection, to avoid oxygen ingress, and to minimise the thermal stresses in the pressure part components during the next restart-up or cold start-up of the plant. An arrangement for injection of auxiliary steam has been provided on the HP side, which allows the drum pressure to remain above the atmospheric pressure while compensating for natural heat losses.

3 WATER-STEAM ANALYSIS AT THE HRSG COLD START-UP

The basic purpose of the analysis was to examine the possibility of preventing the release of steam into the atmosphere through the sky valve during the HRSG cold start-up. Steam emitted into the atmosphere through cross sky valves is not an adequate solution; heat is released into the environment, water is lost and unnecessary additional noise is caused. The possibility of finding a better solution is examined for that reason and the steam quality and possibility of discharging this steam via a new start-up pipeline into the dump condenser is analysed for that purpose.

3.1 HP water-steam quality analysis at the HRSG cold start-up

The HP water-steam analysis was based on a data set obtained from the supervisory control and data acquisition (SCADA) [9]. The data set of the HP water-steam mass flow during the HRSG cold start-up is shown in Figure 11 (a), the HP water-steam temperature during the HRSG cold start-up is shown in Figure 11 (b) and the HP water-steam pressure during the HRSG cold start-up is shown in Figure 11 (c).

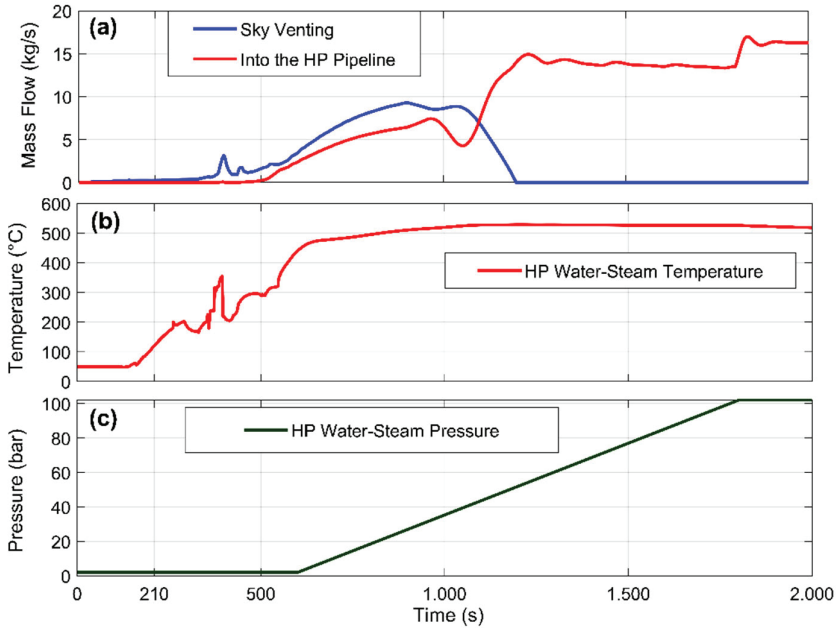

Figure 11: *The HP water-steam data set at the HRSG cold start-up; (a) The HP water-steam mass flow; (b) The HP water-steam temperature, and (c) The HP water-steam pressure*

The HP water-steam density during the HRSG cold start-up into the atmosphere is shown in Figure 12.

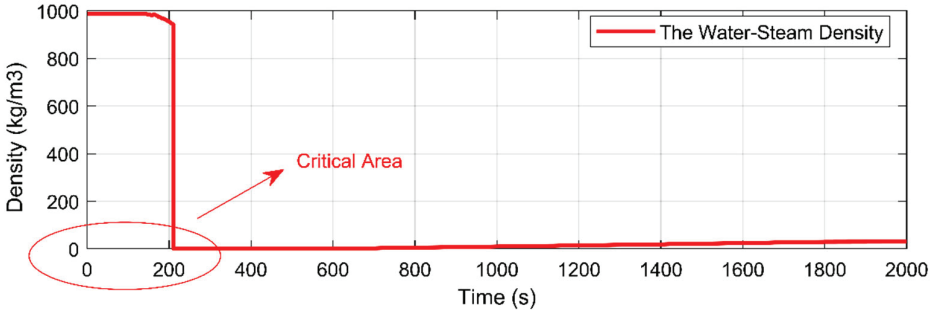

Figure 12: *The HP water-steam density during the HRSG cold start-up*

As shown in Figure 12, for the first 210 seconds from the HP part of HRSG, at the cold start-up, only the water is performed and released, the Critical Area. After 210 seconds the wet steam is generated and is flowing out from the HP part of the HRSG. The formed mixture at this time cannot be transferred either into the steam header or released through sky valves. For the first 210 seconds from the HRSG cold start-up, the HP water and water-steam mixture should be directed into the special blowdown tank, Figure 9. The water-steam density, depending on pressure and temperature, is shown in Figure 13.

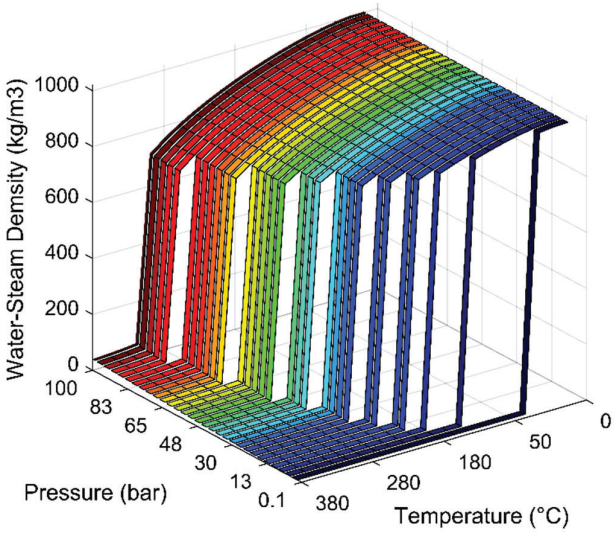

Figure 13: *The HP water-steam density depending on pressure and temperature*

3.2 HP water-steam velocity analysis at the HRSG cold start-up

In the case that the water-steam during the HRSG cold start-up would be discharged into the new start-up pipeline and not released into the atmosphere, the needed pipe diameter has to be calculated so that the steam velocity shall not exceed 50m/s. Several calculations of water-steam velocity were performed for this reason. The water-steam average velocity is dependent on the water-steam density, water steam mass flow, and the pipe`s inner diameter. The following equation was used for the water-steam average velocity calculation [10]:

$$v_a = \frac{4 \cdot \dot{m}_{w-s}}{\pi \cdot \left(\frac{(D_{ou} - 2 \cdot W_t)}{1000}\right)^2 \cdot \rho_{w-s} \cdot n_{pi}} \tag{3.1}$$

where v_a is the water-steam average velocity, $\dot{m}_{w-s}$ is the water-steam mass flow, π is a circular constant, D_{ou} is the pipe outer diameter, W_t is the pipe wall thickness, ρ_{w-s} is the water-steam density, and n_{pi} is the number of pipes. The water-steam density is a function of water-steam pressure and water-steam temperature, and is calculated by a special computer program, Matlab, X-Steam, which can calculate the remaining properties of the steam based on two known thermodynamic properties. The water-steam density is calculated as follows [11]:

$$\begin{matrix} p_{w-s} \\ \longrightarrow \\ T_{w-s} \\ \longrightarrow \end{matrix} \left[\text{XSteam} \right] \begin{matrix} \rho_{w-s} \\ \longrightarrow \end{matrix} \tag{3.2}$$

where p_{w-s} is the water-steam pressure and T_{w-s} is the water-steam temperature. The water-steam velocity in the new start-up pipeline at the different inner pipe's diameters is shown in Figure 14.

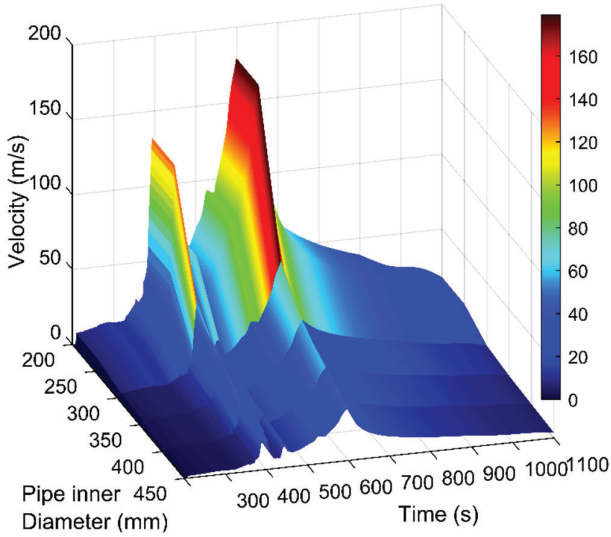

Figure 14: *The water-steam velocity in the new start-up pipeline at the different inner pipes` diameters*

The HP water-steam velocity analysis is based on the HP water-steam properties at the HRSG cold start-up, Figure 11. The HP water-steam analysis, Figure 14, shows that the maximum HP water-steam velocity when the 200 mm pipeline`s inner diameter is 179 m/s, after 600 seconds from the HRSG cold start-up. At the pipe inner diameter of 250 mm, the maximum water-steam velocity was 117 m/s after 600 seconds from the HRSG cold start-up. The maximum velocity of the HP water-steam at the 300 mm pipe inner diameter was 79 m/s, the maximum velocity of the HP water-steam at the 400 mm pipe inner diameter was 45 m/s, and the maximum velocity of the water-steam at the 450 mm pipe inner diameter was 35 m/s after 600 seconds from the HRSG cold start-up.

The HP water-steam results analysis shows that the new start-up pipeline inner diameter should be at least 300 mm. The new start-up pipeline should be horizontal, very long, about 100 m long and, due to the flow of the water-steam mixture in the pipeline, this solution is not recommended. For that reason, it is recommended to integrate a new start-up flash tank into the HRSG system or existing blowdown tank, for which appropriate dimensions can be used. The HP water-steam at the HRSG cold start-up will be discharged into the new start-up flash tank or existing blowdown tank, where the HP water-steam mixture will be separated into the water and the steam. The water will be discharged across the existing blowdown tank into the water tank for district heating, and the steam will be discharged into the low-pressure steam pipe.

3.3 IP water-steam quality analysis at the HRSG cold start-up

The IP water-steam analysis was based on the data set obtained from SCADA. The data set of the IP water-steam mass flow during the HRSG cold start-up is shown in Figure 15 (a), the IP water-steam temperature during the HRSG cold start-up is shown in Figure 15 (b), and the IP water-steam pressure during the HRSG cold start-up is shown in Figure 15st (c).

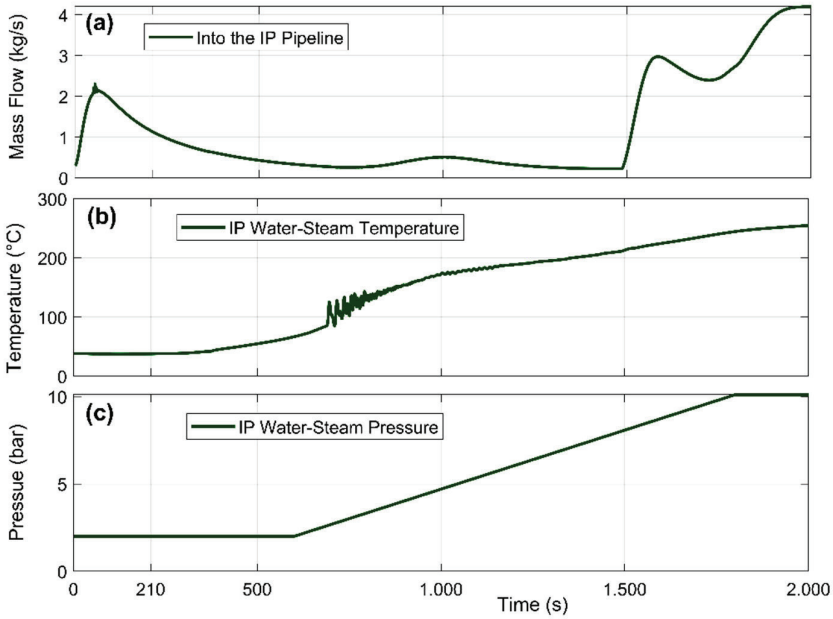

Figure 15: *The IP water-steam data set at the HRSG cold start-up; (a) The IP water-steam mass flow; (b) The IP water-steam temperature, and (c) The IP water-steam pressure*

The IP water-steam density during the HRSG cold start-up into the IP pipeline is shown in Figure 15.

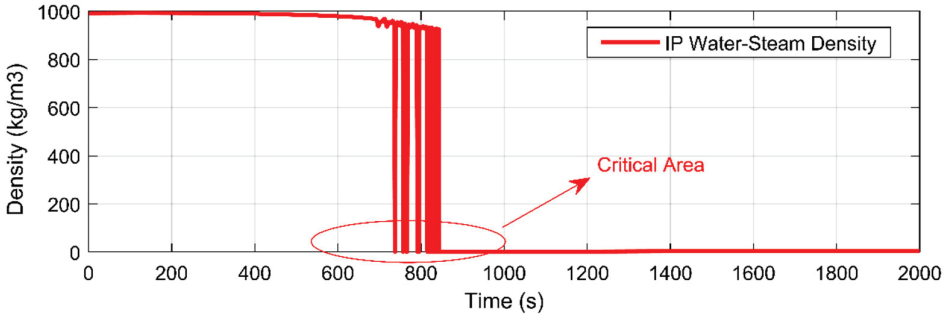

Figure 16: *The IP water-steam density during the HRSG cold start-up*

As shown in Figure 16, for the first 850 seconds, from the IP part of the HRSG, only the water is performed and released, the Critical Area. After 850 seconds from start-up the wet steam is generated and is flowing out from the IP part of the HRSG. The formed mixture at this time cannot be transferred into the IP steam header or into the IP pipeline. In the first 210 seconds from the HRSG cold start, the IP water and water steam mixture should also be directed into the special blowdown tank.

3.4 IP water-steam velocity analysis at the HRSG cold start

The IP water-steam velocity in the IP HRSG project-designed pipeline was analysed at the contractor predicted inner diameter of 204 mm. The IP steam velocity in the 204 mm designed IP pipeline inner diameter is shown in Figure 17.

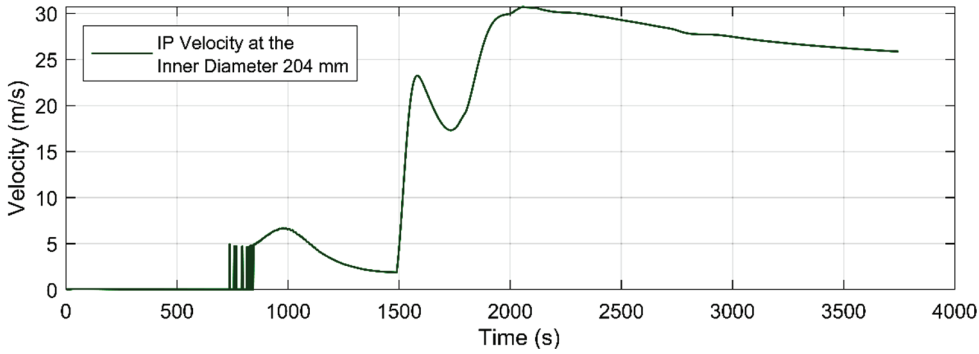

Figure 17: *The IP steam velocity in the 204 mm designed IP pipeline inner diameter*

The IP water-steam velocity analysis was based on the IP water-steam properties at the HRSG cold start-up, Figure 15. The IP water-steam analysis, Figure 17, shows that the maximum IP water-steam velocity at the 204 mm pipeline inner diameter was 31 m/s, after 2050 seconds from the HRSG cold start-up. The IP water-steam velocity analysis shows that the IP pipeline is properly dimensioned. In the first 700 seconds, Figure 16, the HRSG generated only the water; also, the IP pipeline was horizontal and very long, about 100 m, and this water should not be discharged directly into the IP pipeline. Also, at the HRSG start-up, the IP water should be discharged into the special blowdown tank.

4 CONCLUSIONS

The paper presents the HRSG system description in detail and the possibility of preventing the HRSH water-steam-generated release into the atmosphere through the sky valves during the HRSG cold start-up. The water-steam velocity, quality and mass flow from the HP and the IP HRSG parts are analysed during cold start-up. The results show that the first mixture of water and water-steam that is formed in the HP and IP HRSG parts should not be discharged into the HP or IP pipe header. The HP and IP pipelines are mounted horizontally at about 100 m. For that reason, it is recommended that a new start-up flash tank with appropriate dimensions can be integrated into the HRSG system or existing blowdown tank with appropriate dimensions . The water and

water-steam can be separated from the water and the steam. The water can be discharged into the water tank for district heating purposes, and the steam can be discharged into the low-pressure steam pipeline.

References

[1] **J. I. Manassaldi, S. F. Mussati, N. J. Scenna:** *Optimal synthesis and design of Heat Recovery Steam Generation (HRSG) via mathematical programming*, Energy, Vol. 36, Iss. 1, p.p. 475-485, 2011. Available: https://doi.org/10.1016/j.energy.2010.10.017

[2] **A. S. E. Ahmed, M. A. Elhosseini, H. A. Ali:** *Modelling and practical studying of heat recovery steam generator (HRSG) drum dynamics and approach point effect on control valves,* Ain Shams Engineering Journal, Vol. 9, Iss. 4, p.p. 3187-3196, 2018. Available: https://doi.org/10.1016/j.asej.2018.06.004

[3] J. **Li, K. Wang, L. Cheng:** *Experiment and optimization of a new kind of once-through heat recovery steam generator (HRSG) based on analysis of exergy and economy,* Applied Thermal Engineering, Vol. 120, p.p. 402-415, 2017.
Available: https://doi.org/10.1016/j.applthermaleng.2017.04.025

[4] **S. N. Naserabad, A. Mehrpanahi, G. Ahmadi:** *Multi-objective optimization of HRSG configurations on the steam power plant repowering specifications,* Energy, Vol. 159, p.p. 277-293, 2018. Available: https://doi.org/10.1016/j.energy.2018.06.130

[5] **J. F. P. Beaujardiere, H. C. R. Reuter, S. A. Klein, D. T. Reindl:** *Impact of HRSG characteristics on open volumetric receiver CSP plant performance*, Solar Energy, Vol. 127, p.p. 159-174, 2016. Available: https://doi.org/10.1016/j.solener.2016.01.030

[6] **H. Mokhtari, H. Ahmadisedigh, M. Ameri:** *The optimal design and 4E analysis of double pressure HRSG utilizing steam injection for Damavand power plant,* Energy, Vol. 118, p.p. 399-413, 2017. Available: https://doi.org/10.1016/j.energy.2016.12.064

[7] **H. Zebiana, A. Mitsos:** *A split concept for HRSG (heat recovery steam generators) with simultaneous area reduction and performance improvement,* Energy, Vol. 71, p.p. 421-431, 2014. Available: https://doi.org/10.1016/j.energy.2014.04.087

[8] **B. Lesenfants:** *HRSG general arrangement right face,* Contains information for the design of structures, systems and components, Combined cycle power plant, 2020.

[9] Supervisory Control and Data Acquisition (SCADA).
Available: http://www.energetika-lj.si

[10] **D. Chong, W. Liu, Q. Zhao, J. Yan, T. Hibik:** *Oscillation characteristics of periodic condensation induced water hammer with steam discharged through a horizontal pipe, International Journal of Heat and Mass Transfer, Vol. 173, p. 121265, 2021.*
Available: https://doi.org/10.1016/j.ijheatmasstransfer.2021.121265

[11] **D. Strušnik:** *Integration of machine learning to increase steam turbine condenser vacuum and efficiency through gasket resealing and higher heat extraction into the atmosphere,* International Journal of Energy Research, 2021.
Available: https://doi.org/10.1002/er.7375

Abbreviations	(Symbol meaning)
HP	high pressure
HRSG	heat recovery steam generator
IP	intermediate pressure
SCADA	supervisory control and data acquisition

Parameters	(Symbol meaning)
D_{ou}	pipe outer diameter, mm
$\dot{m}_{w-s}$	water-steam mass flow, kg/s
n_{pi}	number of pipes
p_{w-s}	water-steam pressure, bar
T_{w-s}	Water-steam temperature, °C
v_a	water-steam average velocity, m/s
W_t	pipe wall thickness, mm
π	circular constant, 3,14
ρ_{w-s}	water-steam density, kg/m^3

Journal of Energy Technology

JET Volume 14 (2021) p.p. 41-58
Issue 4, December 2021
Type of article 1.01
www.fe.um.si/en/jet.html

DESIGNING AN ELECTROMECHANICAL GENERATOR FOR ENERGY HARVESTING

NAČRTOVANJE ELEKTROMEHANSKEGA GENERATORJA ZA IZRABO ENERGIJE GIBANJA

Franjo Pranjić[R], Nejc Smolar[1], Peter Virtič[1]

Keywords: energy harvest, linear generator, permanent magnets, Finite Element Method

Abstract

Five different designs of tubular electromechanical generator for low frequency energy harvesting have been investigated in this paper. In order to design a simple and robust generator, models were constructed out of permanent magnets, steel and windings. In all five generator models, round movers were used in spherical and cylindrical form- for four models solely permanent magnets were used, and in one model, there was steel present in the mover. The movers are slid or rolled through a tube, and induce voltage in the stator winding. All windings were constructed with the same cross-section dimensions and number of turns. To compare different models, 3D analysis with the Finite Element Method was performed, in order to determine the magnetic flux through the windings. The induced voltage was calculated using the results of the analysis. As a result of the different winding geometries, the average turn length varied for the different designs, subsequently altering resistance and inductance, which affected the generator`s power output and losses. To simulate the generator`s dynamics, an equivalent circuit model was constructed using the Simulink software and data obtained previously from a 3D electromagnetic analysis. With the Simulink model, we coupled the mechanical and electrical systems together to acquire the harvester yields.

[R] Corresponding author: Franjo Pranjić, University of Maribor, Faculty of Energy Technology, Hočevarjev trg 1, 8270 Krško, Slovenija, Email: franjo.pranjic@um.si

[1] University of Maribor, Faculty of Energy Technology

Povzetek

V članku je predstavljenih 5 različnih izvedb cevnega nizkofrekvenčnega elektromehanskega generatorja za izrabo energije gibanja. Z namenom oblikovanja preprostega in robustnega generatorja so modeli sestavljeni iz trajnih magnetov, jekla in navitij. Pri vseh modelih generatorjev sta za okrogli gibljivi del uporabljeni sferična in cilindrična oblika - pri štirih modelih so uporabljeni izključno trajni magneti, pri enem pa je prisotno jeklo. Gibljivi del drsi ali pa se valja skozi cev in pri tem inducira napetost v navitju statorja. Pri vsakem modelu imajo navitja enak presek ter enako število ovojev. Za primerjavo različnih modelov je bila izvedena 3D-analiza z uporabo metode končnih elementov za določitev magnetnega pretoka skozi navitja, na podlagi katerih je izračunana inducirana napetost. Zaradi različnih geometrij navitij se je povprečna dolžina ovoja pri različnih izvedbah spreminjala, kar je posledično spreminjalo upornost in induktivnost ter s tem vplivalo na izhodno moč in izgube generatorja. Za simulacijo dinamike generatorjev je bilo z uporabo programa Simulink in predhodno pridobljenih podatkov iz 3D-elektromagnetne analize določeno nadomestno vezje modela. Za določanje izplena smo z modelom v programu Simulink združili mehanske in električne sisteme.

1 INTRODUCTION

World energy demand is constantly on the rise and, at the same time, there is an urgent demand/need to decarbonise energy production and substitute it with renewable energy. This goal could be achieved easily with the conversion of sea energy, which could replace all current electrical power production [1]. Even though there are 153 coastal countries, only a small amount of energy is currently utilised using sea harvesting, which could capitalise this abundant renewable energy source.

In recent years a lot of research has been done in the field of Sea wave energy exploitation. Different models were developed for energy harvesting, from using piezoelectric, rotational to linear generators, in order to supply grids with renewable energy [2]-[3]. Part of the research has focused on generating power for self-sustainable systems. Sea wave energy harvesting anchored buoys are one of them, where linear generators are used mostly [4]–[7], since they offer high energy density. As diverse as these sea harvesting methods may be, all of them require a fixed anchorage. However, some mobile offshore applications also demand a constant power supply, and with no option to be connected to the power grid, the need arises for self-sustaining systems. Since PV panels are one of more popular choices for self-sustaining applications, due to the abundance of solar energy, such systems are not always the optimal choice, especially as solar powered systems have a big disadvantage in cloudy and foggy conditions and at high latitudes, where daily solar energy during winters is very low. A second problem occurs for cases where the demand for energy is mostly at night time, where expensive energy storages have to be integrated. To minimise energy storage, or even eliminate it, many micro generators have been developed for non-stationary methods of harvesting, normally utilising vibrations or human motions [8]–[15].

The purpose of this article is to create a simple, durable and cost efficient design of a mobile harvester that can generate sufficient electrical energy on the move. The proposed designs of the harvester are constructed only out of a stator, a mover and semiconductors to transform alternating power into direct power .

The stator structure is coreless, which means that there is no iron present. Multiple phase windings are wound on a plastic tube, through which the mover displaces. Two different methods of mover displacement have been used, namely translational, where the friction was minimised by wheels, and rolling motion in the second case, where the mover was rolling on it's outer surface or the surface of the spindles, inducing voltage into the surrounding windings.

A detailed geometrical description of the models, input data, calculation methods, as well geometry analysis with the Finite Element Method is presented in the first part of the article. In the second part, the results of the AC induced voltages at the winding terminals and DC link are presented, and, finally, with help of Simulink simulations, an analysis of the power generation of the harvester coupled with a mechanical model at different loads. Calculations of electrical efficiency and the yield of available energy are performed and the results are compared and discussed.

2 MODELS

The presented sea wave energy harvesters can be divided into two parts. A generating and converting part, where the generating part transforms mechanical energy from the moving part (mover) into electrical energy according to Faraday's law of induction, and the converting part, assembled from semiconductor diodes that convert the alternating voltage to a direct one.

The generating part consists of stationary windings (stator) and a mover, as Fig.1 shows.

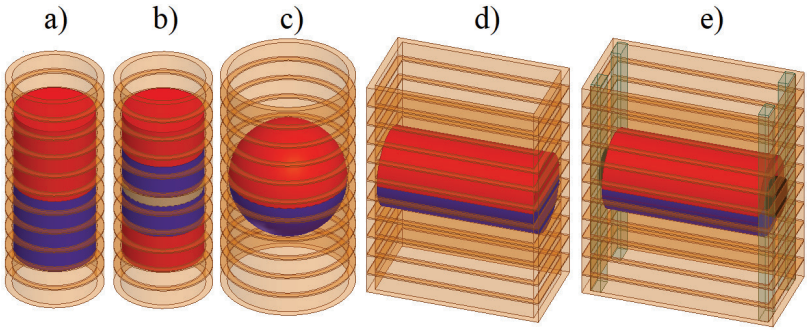

Figure 1: *Energy harvester designs:*
a) Model A - translational cylindrical solid PM mover; b) Model B - translational cylindrical mover with two identical PMs and inserted steel plate in between; c) Model C - rolling spherical mover with solid PM; d) Model D - rolling cylindrical solid PM mover; e) Model E - rolling cylindrical solid PM mover with spindles

Models A and B utilise the translational movement of the cylindrical movers to displace through the stator. Spherical mover C and cylindrical movers D and E use a rolling motion to displace through the stator. The Model C and D movers are rolling on the mover's circumference, and model E's mover is rolling on the circumference of the added spindles, which have been placed on each side concentric to the mover's axis. The basic idea of spindles is to increase the mover's rotational speed in order to increase the magnetic flux change rate.

Movers A, C, D and E are made of single solid two-pole permanent magnets (PM), presented with the red and blue colours in Fig. 1. Model B was assembled from two identical PMs,

between which a steel disc (grey colour in Fig. 1b) was inserted and glued to the PMs. The PMs` magnetisation vectors were facing each other, while the steel disc concentrated the magnetic field to a smaller area, as suggested in [16, 17]. In such an assembly, the mover has three magnetic poles, compared to two poles in the other movers.

A sintered neodymium iron boron (NdFeB) N40 magnet with 1.28 T remanence and -895 kA/m coercivity were used for the PMs` characteristics. The magnets magnetisation vectors were oriented in the displacing direction of the mover, aligned with the coordinate systems Z axis (Fig. 2). The rolling mover's magnetisation vector was, therefore, perpendicular to the mover's rotational axis plane, and was rotating in the XZ plane and displacing along the Z-axis, as sliding movers do.

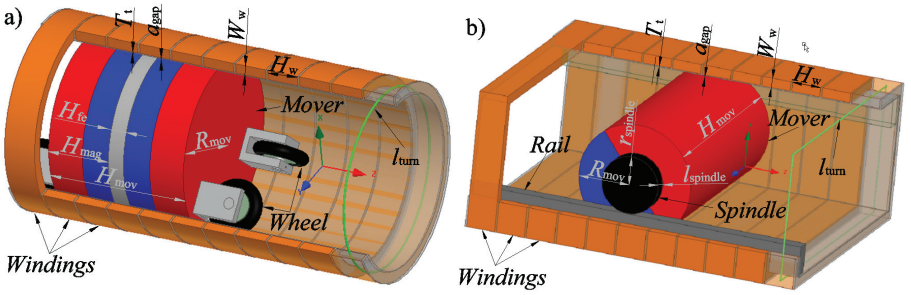

Figure 2: *Schematic harvester/generator structure: a) Model B, b) Model E*

The mass of the movers is identical in all models, 20 kg. This means that, in cases of movers with a single piece PM, the magnet weight is the full 20 kg, and in the case of an assembled mover (model B) each magnet weighed 8.88 kg and the steel plate took up the rest of the mass towards 20 kg, as presented in Table 1.

Table 1: *Harvester designs` parameters*

Symbol	Model				
	A	B	C	D	E
	MOVER				
Mass of the mover m_{mov} (kg)	20	20	20	20	20
Density of the permanent magnet and steel $\rho_{NdFeB} = \rho_{Fe}$ (kg/m^3)	7400	7400	7400	7400	7400
Volume of the mover V_{mov} (cm^3)	2702,7	2702,7	2702,7	2702,7	2702,7
Radius of the mover R_{mov} (mm)	80	80	86,41	50	50
Height of the mover H_{mov} (mm)	134,42	134,42	-	344,12	344,12
Height of the permanent magnet h_{mag} (mm)	134,42	66,09	-	344,12	344,12
Mass of the permanent magnet m_{mag} (kg)	20	2x 8,88	20	20	20

To be continued

Continuation

Height of the steel h_{fe} (mm)	-	15	-	-	-
Mass of the steel m_{fe} (kg)	-	2,23	-	-	-
Length of the spindle $l_{spindle}$ (mm)	-	-	-	-	15
Radius of the spindle $r_{spindle}$ (mm)	-	-	-	-	30
	WINDINGS				
Air gap a_{gap} (mm)	1	1	1	1	1
Tube thickness T_t (mm)	1	1	1	1	1
Height of the winding H_w (mm)	30	30	30	30	30
Width of the winding W_w (mm)	10	10	10	10	10
Filling factor FF	0,6	0,6	0,6	0,6	0,6
Number of turns in one winding N_{turn}	100	100	100	100	100
Length of an average turn l_{turn} (mm)	546,64	546,64	586,92	904,24	964,24
Winding resistance R_w (Ω)	0,51	0,51	0,55	0,84	0,9
Winding inductance L_w (mH)	2,4	2,4	2,64	3,89	4,12

We did not take in to account the mass of the wheels and spindles, which were made of plastic, as they would increase total mass of the movers by less than 1 %. The cylinder`s height was calculated from the defined radius of the movers and the mass of 20 kg, where the same mass density of 7400 kg/m3 was used for the PM and the steel.

We enclosed the movers with a 1 mm thick PVC tube, which provided structural hardness and served as a winding base for the windings. To ensure even spacing for unobstructed movement, a 1 mm air gap was left between the tube and the mover. The general shape of the windings was therefore imposed by the shape of the mover, as shown in Fig. 1. To maximise the magnetic flux, the windings were placed perpendicular to the movement direction in the XY – plane, as shown in Fig. 2. The windings were made of copper wires with 100 turns (Nturn), which were wound concentrically. In the case of model E (the cylindrical mover with spindles) we additionally spread the winding in the Y axis direction to make space for spindles, and rails on which the spindles would roll. The spindles and rails were also made of plastic so as not to disturb th magnetic field or to make any losses due to eddy currents. All windings had the same rectangular cross-section area of 300 mm2, with 30 mm height of the winding (Hw) (Z axis) and 10 mm thickness (Ww). For further calculations, we took a filling factor of 0.6, due to the uncomplicated and simple winding geometry. The windings were spaced 2 mm apart, to leave space for the plastic separation walls, to divide the phases.

To establish equal conditions, all the movers had the same initial kinetic energy, determined by the potential energy of 0.5 m elevation difference (H). We made a presumption that movement in simulations was frictionless, as minimal rolling resistance and low velocities would amount in real conditions to tiny mechanical energy losses.

With this simplification, we could determine the initial velocity of movers A and B, using the simple equation for free falling objects, $v=(g\cdot H)^{0,5}$. For the rolling movers` translational velocities Eq (1) had to be used, where $I$ presents the movers` inertia and m_{mov} presented the mass of mover. In the case of the rolling movers, the radius of the circumferential surface on which mover rolled was presented with the value r_{base}.

$$v = \sqrt{\frac{2 \cdot m_{mov} gH}{m_{mov} + \frac{I}{r_{base}^2}}} \tag{2.1}$$

3 MAGNETIC FLUX AND INDUCED VOLTAGE

An analysis of the magnetic flux through the windings as themover displaced, was performed with 2 mm displacement steps, where the mover displaced by 1.2 m through the tube. All 17 windings were placed onto the tube, which gave 542 mm of total windings` width. The centre of the mass of the ninth winding was placed into the coordinate system centre, so equal amounts of windings were laying on both sides of the coordinate system.

The generator`s geometry was then analysed with ANSYS Maxwell using the 3D magnetostatic Finite Element Method, in order to obtain the magnetic flux and inductivity of the windings. In the case of model B we also checked that the magnetic field density in the steel plate did not reach the saturation point of 1.8 T.

Figs. 3 a) and b) are showing the magnetic flux waveforms of the translational movers. When the mover approaches the observed winding the magnetic flux starts to rise, as a result of more magnetic field lines looping through the winding. When both the mover's and windings' centres of mass were aligned the Dipole PM mover's magnetic flux reached the maximum. In the case of the three pole mover, the magnetic flux reached the maximum when the PM's centre of mass crossed the windings' centre plane, and the magnetic flux dropped rapidly back to zero when the mover's centre of mass reached the windings` centre plane, and changed polarity, due to the opposite magnetisation of the adjacent magnet. From models A and B magnetic flux waveforms, we can see that the waveforms are identical in amplitude and shape, but shifted along the Z axis by the winding's centre of mass distance, which is equal to the sum of the winding's height and the air gap between them.

As we can see from Figs. 3 c), d) and e), the rolling mover's magnetic flux waveforms are more complex. We can view them as a superposition of two motions through winding. The first one is translational and the second one is rotational, where the angle of the constant magnetic field changes relative to the winding's plane as the mover rolls through the tube. Therefore, the magnetic flux changes with the cosine function, where the magnetic flux reaches its highest value when the magnetic field vector aligns with the winding's normal plane, and goes through zero when the magnetic field vector is parallel with the winding`s plane. As a result, the magnetic flux through the windings reaches its maximum and minimum in one full rotation and goes through zero between the extremes every half rotation. Combining the effects of proximity and rotating magnetisation angle, we obtained the displayed magnetic flux waveforms. Comparing Figs. 3 d) and e), we can see that the spindles indeed increased the magnetic flux change rate, as the mover E was forced in to a higher angular velocity, and, therefore, made more revolutions in one pass through the windings.

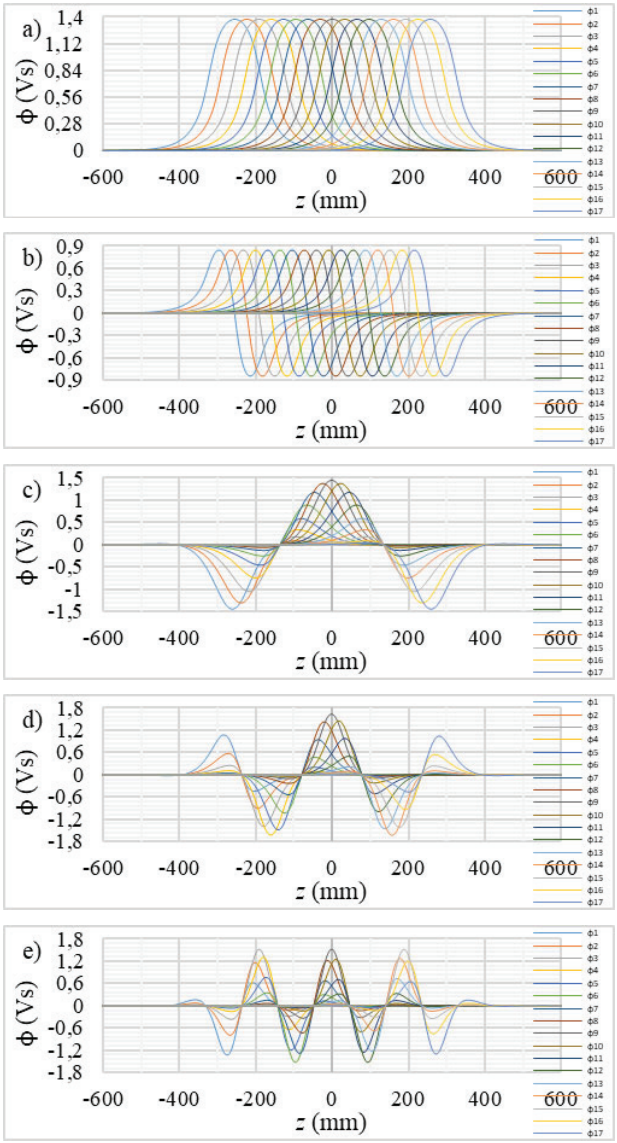

Figure 3: Magnetic flux waveforms: a) Model A, b) Model B, c) Model C, d) Model D, e) Model E

With the defined magnetic flux waveforms for different models we implemented Faraday – Lenz's law of electromagnetic induction e(t)=-dϕ/dt, to calculate the induced voltages in the windings. From the equation for electromagnetic induction we derived Eq (2), which gives the induced voltage in between two positions of the mover's centre of mass at a defined constant velocity. [6]

$$e\left(z_{\mathrm{i}}+\frac{z_{\mathrm{i+1}}-z_{\mathrm{i}}}{2}\right)=-\frac{\left(\varphi\left(z_{\mathrm{i+1}}\right)-\varphi\left(z_{\mathrm{i}}\right)\right)\cdot v}{z_{\mathrm{i+1}}-z_{\mathrm{i}}} \tag{3.1}$$

From the magnetic flux waveforms, using initial velocity, we calculated the induced voltages for the individual windings, to obtain the voltage waveforms, as shown in Fig. 4. To compare the output voltages, we first needed to convert them to direct voltages, with the use of semiconductors arranged in a Greatz bridge.

As result of the different amplitudes of the induced voltages in the windings at the same position of the mover, only the pair of windings with the highest and lowest amplitude would contribute to the voltage output. As the mover progressed through the windings the induced voltages would cross, and the next winding would generate a higher induced voltage and become active.

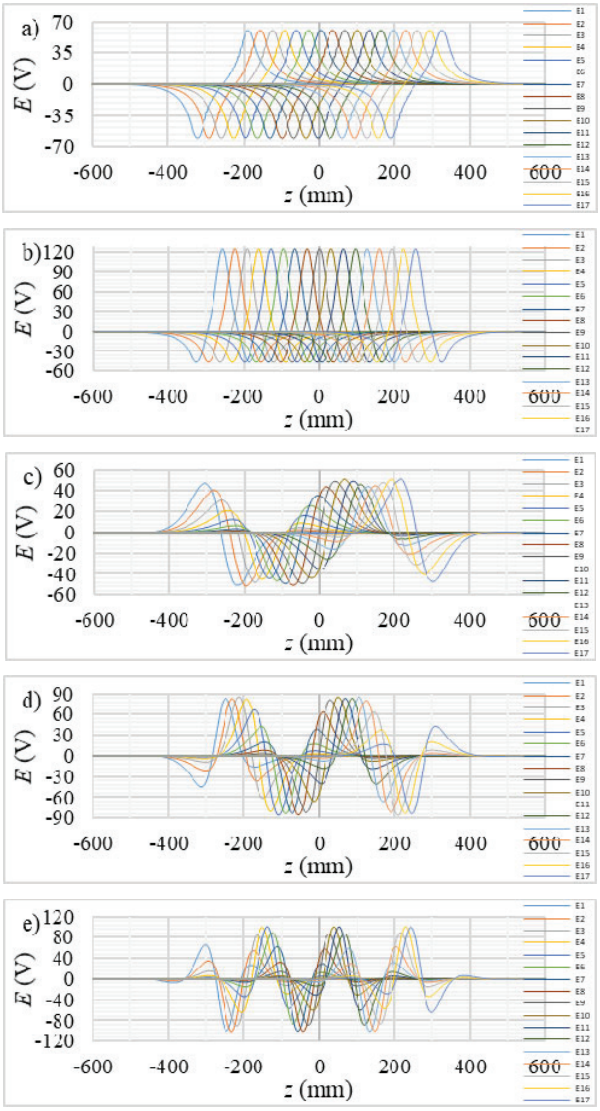

Figure 4: *Induced voltage the waveforms at a constant velocity with the windings wound in the same direction: a) Model A, b) Model B, c) Model C, d) Model D, e) Model E*

Therefore, for transformation into direct voltage at an open circuit, we took the positive and negative extremes at all positions and combined them into positive and negative lines, orange and blue lines as shown in Fig. 5. To get the total potential difference between the positive and negative voltages, we summed the absolute values together, shown by the grey line in Fig. 5.

From the potential difference we calculated the RMS values with Eq 3, to compare the induced voltages for all models on the DC side, in a range from -499 mm to 499 mm,

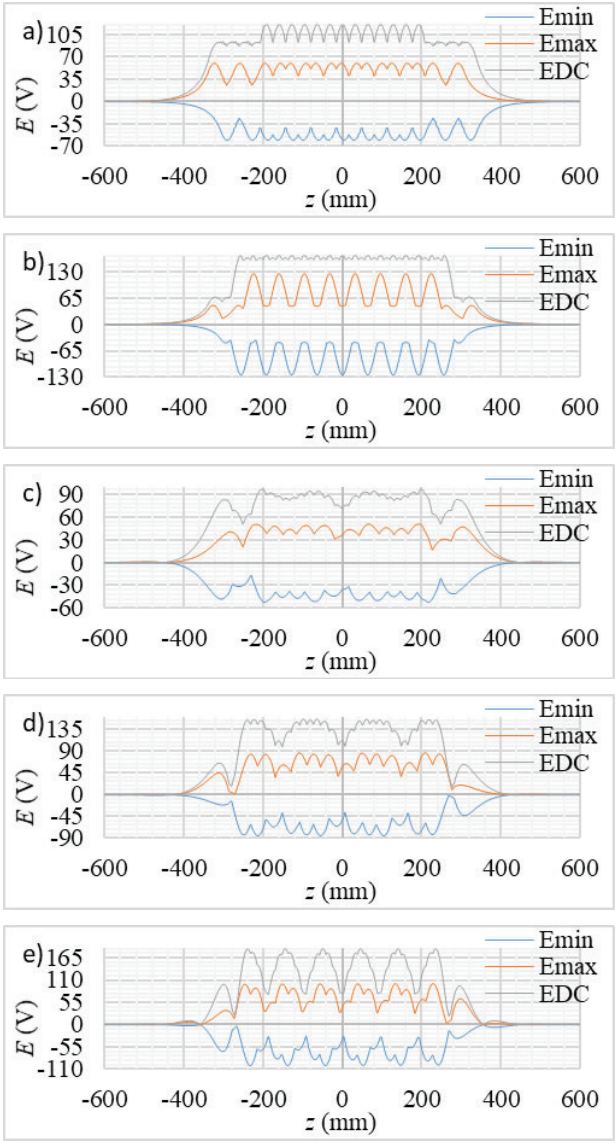

Figure 5: *Direct open circuit voltage at a constant velocity with the windings wound in alternating directions: a) Model A, b) Model B, c) Model C, d) Model D, e) Model E*

$$E_{\text{rms}} = \sqrt{\frac{1}{N}\sum_{\text{n}}(E_{\text{DC}})^2(n)} \tag{3.2}$$

with the translational movers A and B. The design with three poles B scored the highest with 119.48 V, due to the narrow middle pole with a high magnetic flux density. Model A had the second highest RMS voltage of 81.43 V. The rolling cylindrical designs` outputs ranked in the middle, with 69.18 V for model D and 67.04 V for model E. The spherical model had the lowest induced DC voltage of 45.99 V

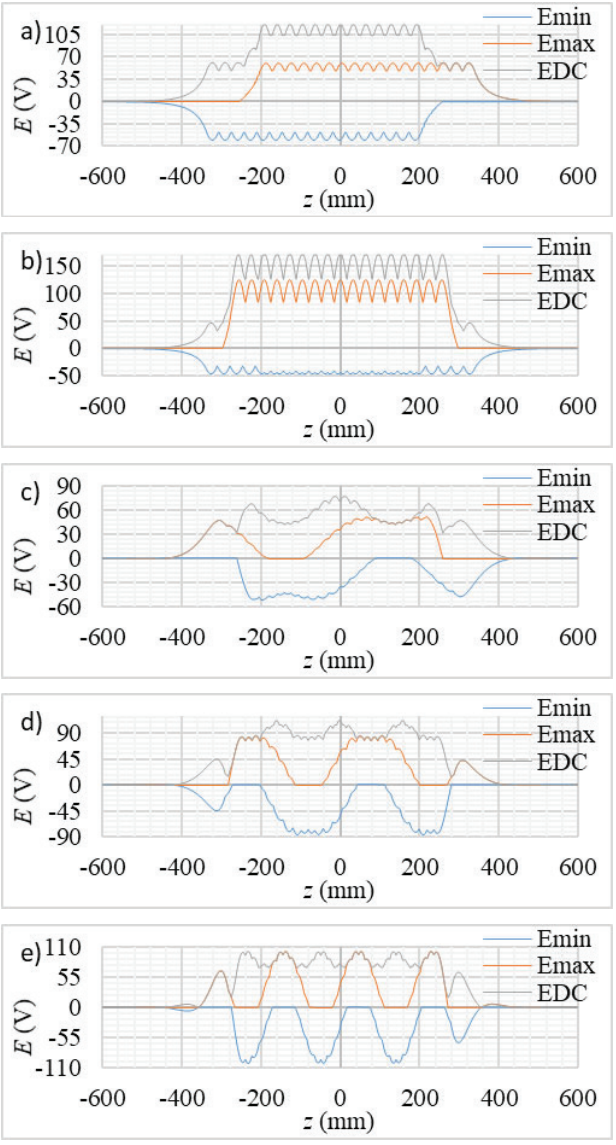

Figure 6: *Direct voltage open circuit at a constant velocity with the windings wound in the same direction: a) Model A, b) Model B, c) Model C, d) Model D, e) Model E*

To create a higher voltage difference on the DC side, the windings were wound alternatingly (Fig. 6) in all models, and the RMS values were recalculated. As the results showed RMS values improved up to 41 % with such windings` configuration, models B, C and E also had smoother induced voltages.

With alternatingly wound windings, the highest improvement was made with the rolling models. The sphere model voltage improved by 25.56 %, resulting in 61.78 V. The second highest improvement was made on D, increasing the RMS induced voltage by 35.55 V, going up to 104.72 V.

The highest improvement on RMS voltage output was made by the cylindrical mover model with spindles, where the voltage increased from 67.04 to 113.49 V. The model with the 3 pole translational mover also improved by about 6.44 %, and still had highest induced voltage on the DC side.

4 SIMULINK MODEL

To research the harvester's operation, we created in Simulink Simscape an equivalent circuit model for the harvester. Each winding was modelled with a resistor, inductor and controlled voltage source. Resistance was determined with the calculated value from the average wire loop length, filling factor and number of turns. Inductance for the windings was obtained from ANSYS, as presented in Table 1.

From the magnetic flux waveforms, the magnetic flux gradients were calculated along z positions, which were used to link the discrete magnetic flux data to the voltage sources. We used dynamic lookup tables, which gave magnetic flux gradients for every 2 mm section. The magnetic flux gradients were then multiplied with the velocity in order to obtain the induced voltages, which were implemented in the circuit with the voltage controlled source. An identical winding circuit was used for all 17 windings with a matching winding magnetic flux gradient, as is shown in Fig. 7.

Figure 7: Direct voltage

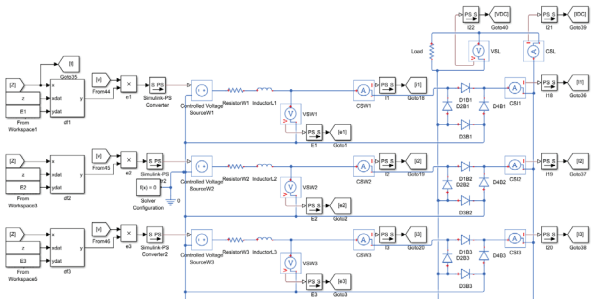

Figure 7: *Part of the harvester equivalent circuit model*

To convert the voltage from alternating to a direct one, we took 17 Greatz bridges, which were connected to the winding terminals. The Greatz bridges were constructed with four diodes, and had default Simscape values of 0.3 Ω. One AC Greatz bridge terminal was then connected directly to the winding terminal and the second terminal was connected to the winding over star/common point connection, which connected all windings together as presented in Fig. 7.

All Greatz bridge DC positive terminals were connected in parallel to create a positive DC link, and negative terminals were connected to the negative DC link. Both DC links were connected with the resistor, which presented the harvester`s load.

The mechanical behaviour of the mover was simulated with the mathematical model, which calculated the velocity of the mover with Eq (4) from the available kinetic energy. To obtain the available kinetic energy at a certain position, the spent energy (Wu) was subtracted, from the constant potential energy (Wp) of 0.5 m, as the law of energy conservation dictates,

$$v = \sqrt{\frac{2 \cdot W_{\mathrm{p}} - W_{\mathrm{u}}}{m + \frac{I}{r_{\mathrm{base}}}}} \tag{4.1}$$

where the spent energy in the system presented the sum of all electrical elements, losses and used energy by load, calculated with the Joule–Lenz law. With the prospect of running one simulation model, we used 0 mechanical inertia for translational movers, as the rest of the equation still holds true.

5 CLOSED LOOP DC LINK VOLTAGE

Fig. 8 shows the harvester's equivalent circuit model DC voltages at 10 Ω load, with the energy conservation law in place. If we compare the open circuit calculated DC voltages, where the movers displaced with constant velocity and amplitudes stayed in the bend, we can see voltage decline comprehensively with the mover's displacement over time, as a result of the velocity decrease.

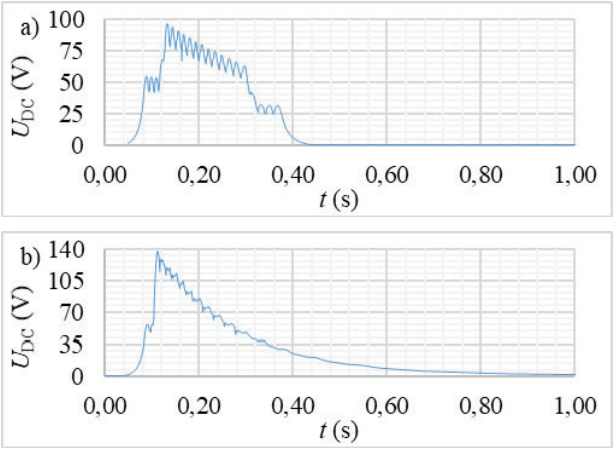

To be continued

Continuation

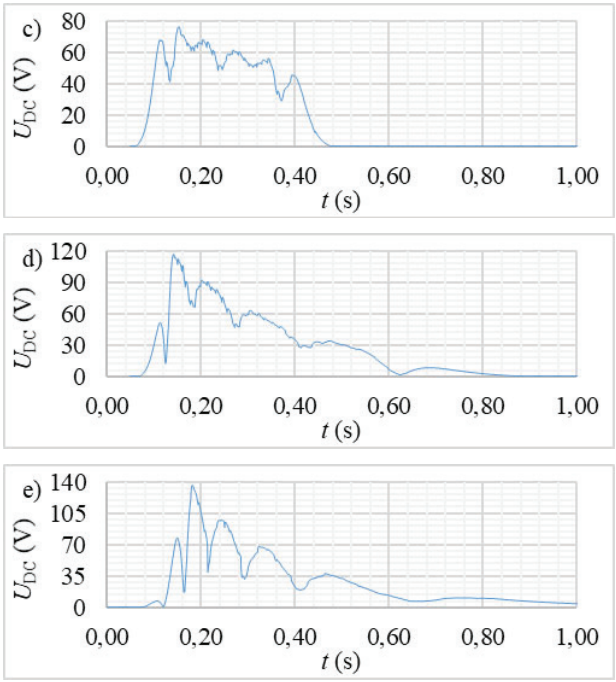

Figure 8: *Equivalent circuit direct voltage at 10 Ω load with alternating wound windings: a) Model A, b) Model B, c) Model C, d) Model D, e) Model E*

In Figs. 8 b), d) and e), where models B, D and E were simulated, we can see that the voltage converged slowly towards 0, until all the kinetic energy was transformed into electrical energy. On the other hand, in Figs. 8 a) and c), the voltage hit 0 steeply at 0.44 and 0.48 s. This can be explained with the velocity, as the movers were still travelling through the tube with high velocities of 1.79 and 1.68 m/s, and the magnetic field displaced too far from the windings to induce voltage, thus induction stopped.

6 KINETIC ENERGY UTILISATION AND ELECTRICAL EFFICIENCY

The goal of all harvesting machines is to extract the highest possible amount of energy. Extraction of energy was, in our case, determined predominantly by the induced voltage and current path resistance. As the winding's geometry and number of turns were fixed, this could be achieved by altering the circuit resistance with load, therefore, we extended the load range from 1 to 15 Ω.

We calculated the percentage of the extracted kinetic energy from the total available energy at the end of the simulation, with 1 Ω increments of loads, as shown in Fig. 9. With increasing load, as Ohms law dictates, current and generated power decreased. Although, too low power generation meant that the mover displaced out of the winding`s induction reach and part of the kinetic energy was not transformed. This is best presented with the mover`s end velocity v' (Fig. 10), which was taken either after displacement of 1.2 m or after 10 s of simulation. Figs. 9

and 10 show clearly, that the load ranges at which full kinetic energy can be extracted differed in all models.

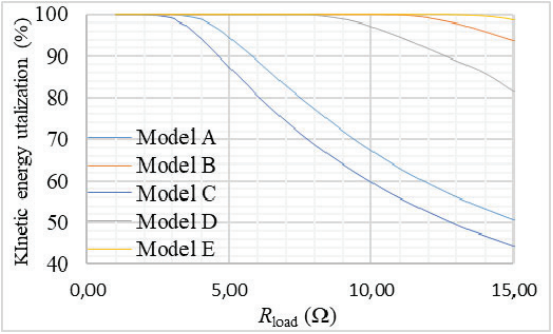

***Figure 9**: Mover`s kinetic energy utilisation*

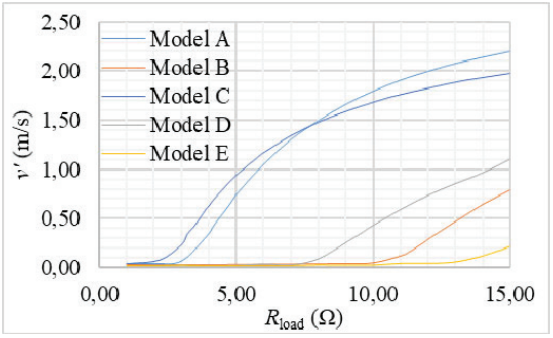

***Figure 8:** Mover velocity at the end of the simulation*

Models A and C, with the lowest induction velocity, had the smallest load ranges of 3 and 2 Ω respectively, of 100% kinetic energy utilisation. Models B and E with higher induced voltages had a wider range of load, which ended at 10 Ω in the case of model B and 14 Ω for model E. The mover in model D ran out of kinetic energy at 8 Ω load. The maximum load coincided inherently with the induced voltage, where models with a higher induced voltage had a wider range of load. This can be explained best with the translational displacing movers (Model A and B curves), that had the same winding resistance and different induced voltages. As the amount of power over time - energy was finite, we could generate a high power output over a short time with low resistance, or a lower power output with a higher resistance over a longer period of time/displacement. However, if the power output would be too low, the mover and magnetic field with it would displace too far away from the windings, so that induction could take place and leftover kinetic energy would go to waste, hence effecting the harvester`s yield.

Moreover, to improve the yield we needed to look from the efficiency perspective as well, as the lost energy from a circuit lowers the harvester`s output, even if all kinetic energy is transformed. Therefore, we calculated the electrical efficiencies in our load range for all models, which we obtained from the ratio between the energy lost on all elements of a circuit and energy consumed by the load. Models (A, B and C) with lower windings` resistances had a much higher electrical efficiency, as did the models (D and E) with higher resistance, as shown in Fig.

associated with lower energy losses in a circuit, as a consequence of smaller resistances of the windings, lower currents and higher energy consumption by the load with increase of load resistance.

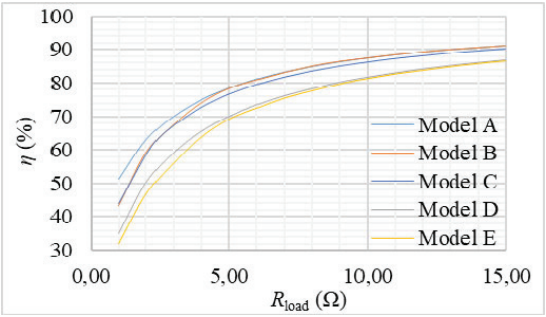

Figure 9: *Equivalent circuit electrical efficiency at a load range from 1 to 15 Ω.*

7 HARVESTER YIELD

As the main feature of energy harvesters is to harness the maximal amount of energy,to transform it into useful electrical energy is as important as the harvesting/extraction itself. When thinking about classical rotational generators, higher efficiency means better transformation of energy. However, in our case, we needed to take into account both efficiency and utilisation, as both affect a harvester`s yield. As the electrical efficiency is increasing, one would suspect that the highest yield would be at the biggest load, at which all kinetic energy is still utilised.

With the prospect of determining the best solution from the chosen designs, our objective was to find the highest yield point of each design to compare them to each other. For this reason, we ran simulations with different resistive loads at the same kinetic energy input for all presented models, trying to find a balance between losses and gains through utilisation of the whole generator length.

Energy yield was, therefore, determined with the ratio between kinetic energy on disposal and the energy used by the load.

$$yield = \frac{W_{\text{load}}}{W_{\text{k}}} \cdot 100 \tag{7.1}$$

To determine the highest yield point and at which load it occurs precisely, we calculated the yields with increments of 0.1 Ω, moving away from the previously obtained highest value of yield for ±1 Ω.

As **Napaka! Vira sklicevanja ni bilo mogoče najti.** shows, the maximum yield points were slightly pushed into higher loads as 0 end velocities were occurring. Model A, with a translational solid PM mover maximum yield was, at 4.5 Ω load, 74.52 %. The harvester with rolling spherical PM mover had 5.79 % lower maximum yield at 4 Ω. Model D, with the rolling cylindrical PM, had the highest yield of 79.69 % at 9.6 Ω. Harvesters B and E were the only ones which were operating above 80% yield already at 6 and 9.5 Ω, respectively. Model E had

reached a yield of 85,58 % at 14.7 Ω, and the absolute highest yield of 88,76 % was achieved by the composited mover made from PM and the steel plate, at 11.8 Ω.

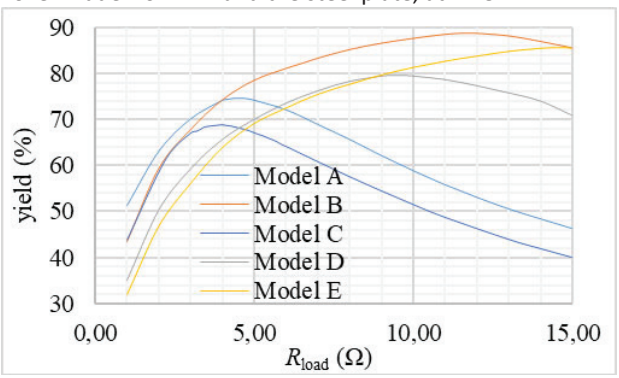

Figure 10: Equivalent circuit yield at load range from 1 to 15 Ω

For harvesters B and E we extended the load further, so that we could determine the range of the load, where both harvesters would yield more than 80 %. The B model`s last load over 80 % was at 18 Ω, where, for models E, it was at 20.4 Ω, which could be considered advantages, as loads could vary more than 5 Ω and the harvesters would still have reasonably good yields.

8 CONCLUSIONS

Hoping to create feasible and simple designs of an electromagnetic harvester, five proposed geometries were analysed, to determine the design with the highest yield.

Firstly, the magnetic flux waveforms and inductivity were calculated with the magnetostatic FEM in ANSYS. The same mass was used for all movers, although the shapes and displacement methods varied. Two movers were displacing translationally, and the other three were rolling throughthe stator, whereby one mover was forced into a higher angular velocity by spindles added on the sides of the mover. As a result of the different movers` geometries the windings had to be adjusted, although the windings` cross-sections stayed identical. From the magnetic flux waveforms, open circuit induced voltages were calculated at a constant centre of mass velocity, where the velocities were derived from kinetic energy, which was determined with the potential energy of 0.5 m.

Two winding configurations were calculated to find the highest induced voltage winding. The first configuration had all windings wound in the same direction and connected into a star connection. In the second winding configuration, the windings were wound in alternating directions, which turned out to be better configurations in all models, due to the higher induced voltages` potential differences.

An equivalent circuit model was constructed in Simulink and dynamic of harvester was simulated to conduct further evaluations. The mathematical part of the model calculated the velocity of the mover as it progressed through harvester, from the available kinetic energy, which was determined from the initial mover`s energy and electrical losses that accumulated over the time of displacement. The physical part, modelled with Simscape, presented the

windings, converter and load. The windings were modelled with a resistor, an inductor and a voltage source, which was driven by the magnetic flux gradient calculated in ANSYS and the velocity from the mathematical model. The converter part was modelled with four diodes in a Greatz bridge arrangement and converted windings AC to DC. The DC terminals of the converters were connected in parallel to establish positive and negative DC links. The DC links were connected with an ohmic load.

To determine the highest yield for every design, an array of simulations was conducted with loads from 1 to 15 Ω. As the results show, every harvester had a different optimal point of yield, as well as the highest yield itself. Models with higher induced voltages tended to have better yields, up to 85 %, compared to ones with lower induced voltages, regardless of their inner resistance and inductance. With higher voltages, as load resistance increased, more power could be shifted towards the load, as circuit losses decreased and efficiency improved, when still being able to convert all kinetic energy into electrical energy. Although as it turned out, maximum points of yield did not occur in a range of loads where all kinetic energy was spent, but slightly after, where a small part of the kinetic energy was still left in the mover.

Moreover, the design with the cylindrical translational mover with the concentrated magnetic flux pole and a rolling mover on spindles, which had the highest induced voltages, were able to operate over 80 % of yield at a high range of load, which could prove to be beneficial for harvesters with variable load or variable inbound mover velocity.

References

[1] **M. A. Mueller**: *Electrical generators for direct drive wave energy converters*, IEE Proceedings - Generation, Transmission and Distribution, vol. 149, no. 4, pp. 446-456, July 2002. Available: https://digital-library.theiet.org/content/journals/10.1049/ip-gtd_20020394

[2] **R. Alamian, R. Shafaghat, S. Jalal Miri, N. Yazdanshenas, M. Shakeri**: *Evaluation of technologies for harvesting wave energy in the Caspian Sea*, Renewable and Sustainable Energy Reviews, Volume 32, 2014. Available: https://doi.org/10.1016/j.rser.2014.01.036

[3] **Y. Cui, Z. Liu:** *Effects of Solidity Ratio on Performance of OWC Impulse Turbine*. Advances in Mechanical Engineering. January 2015. Available: https://doi.org/10.1155/2014/121373

[4] **S. Hor, A. Tabesh and A. Zamani**: *Analytical model of an improved linear generator for seawave energy harvesting,* IET Conference on Renewable Power Generation (RPG 2011), 2011, pp. 1-4, Available: https://doi: 10.1049/cp.2011.0230

[5] **A. Pirisi, M. Mussetta, F. Grimaccia, D. Caputo, G. Gruosso and R. E. Zich:** *An innovative device for traffic energy harvesting*, 6th IET International Conference on Power Electronics, Machines and Drives (PEMD 2012), Bristol, 2012, pp. 1-6. , Available: https://doi: 10.1049/cp.2012.0337

[6] **H. Li, P. Pillay:** *A Methodology to Design Linear Generators for Energy Conversion of Ambient Vibrations*, *2008 IEEE Industry Applications Society Annual Meeting*, 2008, pp. 1-8, Available: https//doi: 10.1109/08IAS.2008.72

[7] **L. Huang, J. Liu, H. Yu, R. Qu, H. Chen, and H. Fang:** *Winding configuration and performance investigations of a tubular superconducting flux-switching linear generator*, IEEE Trans. Appl. Supercond., vol. 25, no. 3, 2015. Available: https://doi: 10.1109/TASC.2014.2382877

[8] **G. Bracco, E. Giorcelli, and C. Attaianese:** *Design and experiments of linear tubular generators for the Inertial Sea Wave Energy Converter*, 2011 IEEE Energy Conversion Congress and Exposition, 2011, pp. 3864-3871, Available: https://doi: 10.1109/ECCE.2011.6064294

[9] **J. Asama, M. R. Burkhardt, F. Davoodi and J. W. Burdick:** *Investigation of energy harvesting circuit using a capacitor-sourced buck converter for a tubular linear generator of a moball: A spherical wind-driven exploration robot*, 2015 IEEE Energy Conversion Congress and Exposition (ECCE), 2015, pp. 3167-3171, Available: https:// doi: 10.1109/ECCE.2015.7310104

[10] **M. R. Burkhardt, F. Davoodi, J. W. Burdick, and F. Davoudi:** *Energy harvesting analysis for Moball, A self-propelled mobile sensor platform capable of long duration operation in harsh terrains*, Proc. - IEEE Int. Conf. Robot. Autom., pp. 2665–2672, 2014. Available: https://doi: 10.1109/ICRA.2014.6907241

[11] **S. Wu, P. C. K. Luk, C. Li, X. Zhao and Z. Jiao:** *Investigation of an Electromagnetic Wearable Resonance Kinetic Energy Harvester With Ferrofluid*, IEEE Transactions on Magnetics, vol. 53, no. 9, pp. 1-6, Sept. 2017, Art no. 4600706, Available: https://doi: 10.1109/TMAG.2017.2714621

[12] **N. Fondevilla et al:** *Electromagnetic harvester device for scavenging ambient mechanical energy with slow, variable, and randomness nature*, 2011 International Conference on Power Engineering, Energy and Electrical Drives, 2011, pp. 1-5, Availbale: https://doi: 10.1109/PowerEng.2011.6036432

[13] **J. Asama, M. R. Burkhardt, F. Davoodi and J. W. Burdick:** *Design investigation of a coreless tubular linear generator for a Moball: A spherical exploration robot with wind-energy harvesting capability,* 2015 IEEE International Conference on Robotics and Automation (ICRA), 2015, pp. 244-251, Available: https//doi: 10.1109/ICRA.2015.7139007

[14] **B. J. Bowers and D. P. Arnold:** *Spherical, rolling magnet generators for passive energy harvesting from human motion*, J. Micromechanics Microengineering, vol. 19, no. 9, 2009. Available: https:// doi:10.1088/0960-1317/19/9/094008

[15] **J. Joos and O. Paul:** *Spherical magnetic energy harvester with three orthogonal coils*, 2015 IEEE SENSORS, 2015, pp. 1-4, Available: https://doi:10.1109/ICSENS.2015.7370662

[16] **C.R. Saha, T. O'Donnell, N. Wang, P. McCloskey:** E*lectromagnetic generator for harvesting energy from human motion*, Sensors and Actuators A: Physical, Volume 147, Issue 1, 2008, Pages 248-253, Available: https://doi.org/10.1016/j.sna.2008.03.008

[17] **F. Pranjić, P. Virtič:** *Determination of an Optimum Fictitious Air Gap and Rotor Disk Thickness for a Coreless AFPMM*, Tehnicki Vjesnik, Vol. 25(6):1731-1738, December 2018, Available: https://doi:10.17559/TV-20171109105213

Journal of Energy Technology

JET Volume 14 (2021) p.p. 59-67
Issue 4, December 2021
Type of article 1.01
www.fe.um.si/en/jet.html

METHODOLOGY OF IMMERSIVE VIDEO APPLICATION: THE CASE STUDY OF A VIRTUAL TOUR

APLIKACIJA IMERZIVNIH VIDEO METOD: PRIMER VIRTUALNEGA OGLEDA

Jure Jazbinšek[R], Gorazd Hren[1]

Keywords: virtual tour, 360 camera, RICOH THETA Z1, 3dVista, Text to Speech

Abstract

A Virtual Tour is an interactive presentation of real places accessible directly with an Internet browser with no additional installations of apps of plugins. Once, 360° photos are recorded and processed (stitched into spherical panoramas), editing of a Virtual Tour (walk) enables connection of spherical panoramic photos (or videos) into interactive presentations. For an enhanced experience and stand-alone presenting ability, features are added, like natural-sounding voice for text-to-speech descriptions and embedded videos. During multiple virtual tour presentations, users, viewers and presenters reported exceptional usability and an immersive experience. Virtual Tours have great potential to reshape the future education process and establish a new benchmark for presentation. The Virtual Tours application is expected to be used in education, tourism and future building sites or industry, as a key component for workforce briefings, and "as build" documenting of various stages of build, with the possibilities to integrate into Building Information Modelling (BIM) models.

[R] Corresponding author: Jure Jazbinšek, GEN energija, d.o.o., Vrbina 17, 8270 Krško, Slovenija, tel: + 386 7 49 10 112, Email: jure.jazbinsek@gen-energija.si

[1] Faculty of Energy Technology, University of Maribor, Hočevarjev trg 1, Krško, Slovenia

Povzetek

Virtualni ogled je interaktivna predstavitev resničnih krajev, dostopnih neposredno z internetnim brskalnikom brez dodatnih namestitev aplikacij ali kakršnihkoli vtičnikov. Ko so 360 -stopinjske fotografije posnete in ustrezno obdelane, sledi urejanje virtualnega ogleda (sprehoda), ki omogoči povezavo sferičnih panoramskih fotografij (ali videov) v interaktivne predstavitve. Za boljšo izkušnjo in samostojno predstavitev je posameznim panoramam dodan naravni zvok glasu, ki opisuje prostor ali predstavi željeno področje. Po večkratnih predstavitvah uporabniki, gledalci in predstavitelji poročajo o izjemni uporabnosti platforme. Virtualni sprehod ima zaradi poglobljene izkušnje velik potencial za preoblikovanje novodobnega izobraževalnega procesa in vzpostavitev novih meril predstavljanja. Pričakuje se, da se bodo virtualni ogledi uporabljali predvsem v izobraževanju, turizmu, na gradbiščih prihodnosti ter v industriji kot ključna tehnologija za napotke delovni sili in dokumentiranje različnih stopenj gradnje in razvoja z možnostjo vključitve posnetkov v modele gradbenega informacijskega modeliranja (BIM).

1 INTRODUCTION

The COVID-19 pandemic has had a significant impact on all sectors of business. The development of the information society and the universal access to modern technologies have resulted in a new form of participation in business. The creation of virtual space may take place using several forms of presenting data and publishing them on the Internet. These include exploring the virtual spaces through geoportals (including 3D geoportals), Virtual Tours and electronically accessible videos, which are appropriate for the information societies.

In this paper we are focused on Virtual Tours, also called virtual walks. Studies on and explanations for this issue are available mainly on the Internet. In the literature [1-4] authors understand them as multimedia presentations containing high quality panoramas, thanks to which it is possible to see a given place as close to reality as possible. The viewer can look around, admire the perspective and specific details, move between specific locations, zoom in or out and move in selected directions. The purpose of this form of presentation is to give the user the impression of being in each place. Thanks to the use of multimedia solutions, it is possible to attach voice and text effects. The development and evaluation of a Virtual Tour prototype were performed mainly for tourist destinations [2,5] (museums, sightseeing, etc.).

In the new, COVID-19 time, the Education and every-day Communication has taken a sudden swing towards digitalisation. The established routines of standard meetings and classroom presentations were not possible during lockdown periods. A few new platforms for communication have arisen, but for presenting anything to partners or students, MS PowerPoint is still a standard. With the lowering cost of 360 photography and more processing power and connectivity, new platforms for 3D Virtual Tours have risen to their potential. The option to simplify the process of taking high-quality 360° photos, edit them, arrange them in a Virtual Tour, add interactive features and attach media files and publish them, is still a semi-complicated process. New 3D editing programs that will enable simplification of this process will establish a new sandbox for education, presentation of infrastructure and equipment and other fields of use.

Panoramic, or wide format photographs, are pictures that depict horizontally elongated fields of view, or pictures that depict a field of view that is wider than the natural human field of view. It

can be classified into 3 types: The cylindrical, spherical/cubical and planar panoramas, and all 3 types can be either conventional 2D or stereoscopic.

Spherical panoramas are used for virtual-reality purposes, and they show the entire field of view from a single point, 360° horizontally and 180° vertically, allowing the viewer to look in every direction. The image is wrapped into a sphere and viewed from the centre. The horizontal and vertical directions of a spherical panorama are

distorted when flattened. A spherical panorama can be flattened and stretched to become cubic, each cube face representing a planar image that looks normal to the human eye.

Cylindrical panoramas, used primarily in stills photography, depict a 360° horizontal field of view that has vertical constraints, depending on the equipment used or the editing of the image. If flattened out, straight horizontal lines become curved, while straight vertical lines remain straight. There are two types of cylinder panoramas. In the case of inner-cylinder panoramas the setting of the camera stays fixed, and the picture is captured by rotating the 360° camera. In the case of outer-cylinder panoramas the subject is kept fixed and the camera takes photos of the whole circle of the subject. A cylindrical panorama is intended to be viewed as if it were wrapped into the shape of a cylinder and viewed from within.

A Planar panorama is a panoramic photo that is produced by the combination of a series of frames. This method is used mainly in cases where the other two methods cannot be used (e.g. streets or building groups). The camera is positioned halfway along the subject until the whole subject is captured.

Stereoscopic photos are pairs of images, taken simultaneously with two lenses corresponding to the two human eyes, looking in the same direction. When viewed with a stereoscope, such as a View Master, these images create an impression of depth and solidity, and give viewers the impression of seeing a 3D space. This can be applied to the case of panoramas of any type, with the combination of a pair of 360° images, which, when viewed with synchronised Panorama viewers, present a stereo pair. The most popular stereoscope for viewing stereo panoramas is a virtual reality headset.

1.1 Virtual Tours

A Virtual Tour is a simulation of an existing area, usually composed of a sequence of still images or videos, showing the geometrical properties of the location, and supplying information via multimedia, giving users a wrap-around feeling and the impression that they are navigating locations and experiencing them in real time [6]. In using techniques and characteristics that represent a location accurately, namely the exact depiction of all entities (e.g., buildings, objects, facilities), the precise layout, and a high level of interactivity with the user to control and navigate in the virtual environment freely, a virtual tour can manage to provide the user with an experience similar to visiting the real location. Design guidelines for immersive video applications, with an application example, are listed in [7] for a cultural heritage virtual tour.

Google Street View is an innovative Virtual Tour application that was launched by Google in May 2007, can be found in both Google Maps and Google Earth, and provides 360° horizontal and 290° vertical panorama street level views of the surrounding area of a certain spot.

It is a creation of interactive 360º virtual tours with 360º views (panoramas), 360º videos, embedded sounds, videos and photos, floorplans and fully customisable frames. It has the ability of presenting the recorded space with multifunctional hotspots and clickable objects that the audience can explore when walking through the tour. Virtual Tours can be seen on any computer, tablet, or phone (Android & iOS) - no installation or plugins are needed, Online or Offline, they are VR compatible. The application has shown enormous usability during the time of restricted gatherings due to COVID-19 restrictions, and was used twice for the purpose of presenting Faculty laboratories to future students.

2 HARWARE FOR 360° PHOTOS

The Full Spherical Camera model RICOH THETA Z1 presented in *Figure 1* was used for shooting Virtual Tours.

Figure 1: *Full Spherical Camera model RICOH THETA Z1*

The camera is capable of shooting videos with 4K resolution (3840×1920 with 30 FPS). It has an internal memory of 19 GBs, which can store 350 photos in RAW format, 2400 photos in JPEG format or 40 minutes of 4K video (max. 5 minutes time per recording). The full specifications of the RICOH THETA Z1 are presented in Table 1 [8].

Table 1: *Specifications of the Full Spherical Camera model RICOH THETA Z1 [2]*

Name of product:	RICOH THETA Z1
Lens F number	F2.1, 3.5, 5.6
Object distance	Approx. 40 cm - ∞ (from the front of the lens)
Image Sensor Size	1.0- inch type (x2)
Image Sensor Effective Pixels	Approx. 20 M (x2)
File Size Still Images	RAW: 7296×3648 JPEG: 6720×3360
File Size Videos	4K: 3840×1920/29.97 fps/56 Mbps 2K: 1920×960/29.97 fps/16 Mbps
File format	Still image: RAW (DNG)*2, JPEG (Exif Ver. 2.3)Video: MP4(Video:MPEG-4 AVC/H.264,Audio: AAC-LC (monaural) +Linear PCM (4ch Spacial audio))Live Streaming: Video: H.264, Audio: Linear PCM (4ch)
Recording medium	Internal memory: Approx. 19GB
Number of photos that can be recorded, time	Still image: RAW+ Approx. 350 photos, JPEG Approx. 2400 photosVideo (time per recording): Max. 5minutes/Max. 25 minutes*3*4Video (total recording time): (4K) Approx. 40 minutes, (2K) Approx. 130 minutes
Shooting mode	Still image, Video: Auto, Aperture priority, Shutter priority, ISO priority, Manual*3Live Streaming : Auto
Shooting Functions	Still image: Noise reduction, DR compensation, HDR Rendering, Interval

To be continued

Continuation

	shooting, Interval Composite shooting, Multi bracket shooting, Self-timer (2, 5, 10 sec.), MY SettingsVideo: Self-timer (2, 5, 10 sec.), MY Settings
OLED Panel	0.93 inch Organic Light Emitting Display Panel,128x36 dots, Automatic brightness adjustment function
Wireless Communications Standard	IEEE802.11 a/b/g/n/ac (2.4 GHz/5 GHz)*5, IEEE802.11 b/g/n (2.4 GHz Only), Bluetooth 4.2
External interface	USB Type-C, USB3.0
Power source	Lithium ion battery (built in)
Battery life	Still image: Approx. 300 photos*7 Video: Approx. 60 minutes*7
Exterior/external dimensions	48 mm (W) x 132.5 mm (H) x 29.7 mm (24 mm)
Weight	Approx. 182 g
Usage temperature range	0°C - 40°C

The camera has two image sensors, and was set with custom macro to shoot multiple (4) snapshots for every location: 1x JPEG (6720×3360 pixels) and 3 snapshots in RAW mode (7296×3648 pixels). The recorded 360°snapshots were merged in the program Adobe Lightroom, in order to achieve more realistic colours, and, finally, stitched into a single spherical 360° photo with the specially dedicated 3dVista plugin software.

3 SOFTWARE FOR THE CREATION OF A VIRTUAL TOUR

The Multimedia Virtual Tour was created with the software 3dVista VIRTUAL TOUR PRO, which enables stitching 360°panoramas and connecting multifunctional hotspots and clickable objects that a user discovers when walking through the tour.

A Virtual Tour lets you see a place on the screen in a way that is most like experiencing it in real life. Virtual Tours can generally contain many different types of media and tools, such as photos, panoramas, videos and audio. Technically, a Virtual Tour is the transformation of a flat panorama image into a spherical format. The Virtual Tour allows the viewer to walk virtually through the recorded scenery using his computer, TV or mobile phone. Within this Virtual Tour you can show panoramas, videos, photos, floor plans or maps, and you can play different sounds, depending on where your viewer looks (immersive audio).

The 3dVista Virtual Tour Suite enables creation and publishing of spherical Virtual Tours that will give viewers the impression of being in the room. They can then pan around, look up, down, left and right, and feel like they are actually in the middle of the scene. On top of that, you can add interactivity, audio, photos, videos and much more, to enrich the experience. [9]

Once, 360° panoramas of laboratories were merged from 3 360° photos with various exposure times, colour corrected in Adobe Lightroom and stitched, but now, the assembly of a Virtual Tour takes place in 3dVista VIRTUAL TOUR PRO. Hotspots buttons (clickable objects) that connect panoramas should be added to define transitions between the presented content (another panorama, text, video, …) – an example of the workflow of 3dVista VIRTUAL TOUR PRO, where hotspots between panoramas are edited, is presented in Figure 2.

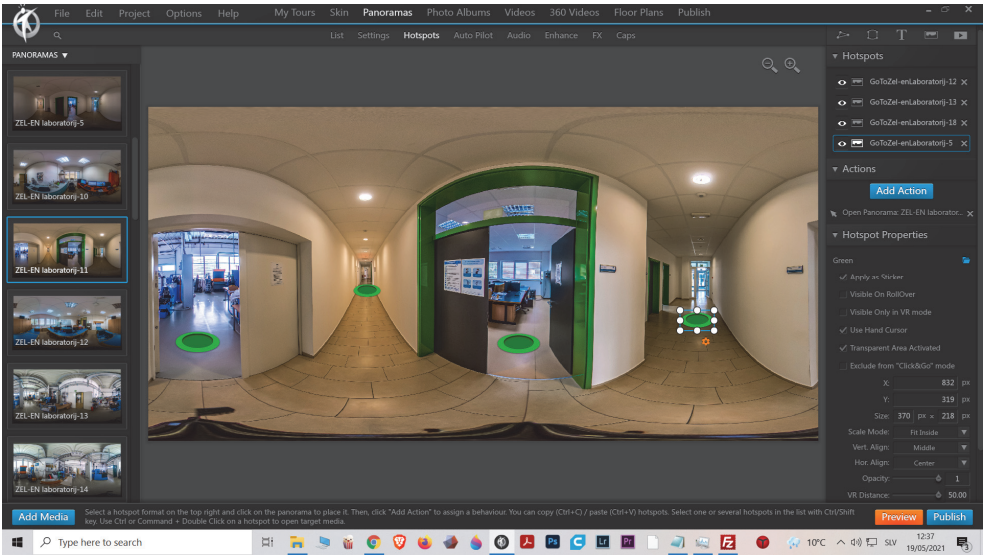

Figure 2: *Example of the workflow of the 3dVista VIRTUAL TOUR PRO*

4 TEXT TO SPEECH

The Text to Speech Feature converts any written text inside your Virtual Tour into spoken words, so it reads digital text aloud. This is not only useful in terms of Web accessibility, where alt text options are essential for people with disabilities, such as blindness or dyslexia. It's useful for all Virtual Tour visitors. Content can be read aloud for people who prefer to listen, for example, while navigating the tour rather than having to stop and read a whole lot of text. This is particularly useful for users exploring the Virtual Tour in VR or AR headsets, which are simply not meant for reading texts.

4.1 3D Vista Text to Speech

The Text To Speech feature can be applied to all sorts of text you can find in a Virtual Tour. It can read out info window texts, tool tips, buttons, or even play an audio description of the current media, within a panorama, or even a 360º video. [10]

4.2 MS Office Text to Speech

Speak is a built-in feature of Word, Outlook, PowerPoint and OneNote. You can use Speak to have text read aloud in the language of your version of Office. Text-to-speech (TTS) is the ability of your computer to play back written text as spoken words. Depending upon your configuration and installed TTS engines, you can hear most text that appears on your screen in Word, Outlook, PowerPoint and OneNote. For example, if you're using the English version of Office, the English TTS engine is installed automatically.

MS Office Text To Speech offers reading in the Slovenian language (Pregled / Govor / Glasno branje) with the voice option name Microsoft Lado, and only the most basic option of adjusting the speed of reading is available.

4.3 MS Azure Text to Speech

There are some limitations with the supported languages in the Text To Speech Feature and the Slovenian language is not yet supported as an option. This challenge was solved with the Microsoft Azure - Text to Speech demo application, built on JavaScript SDK and available free online. [11]

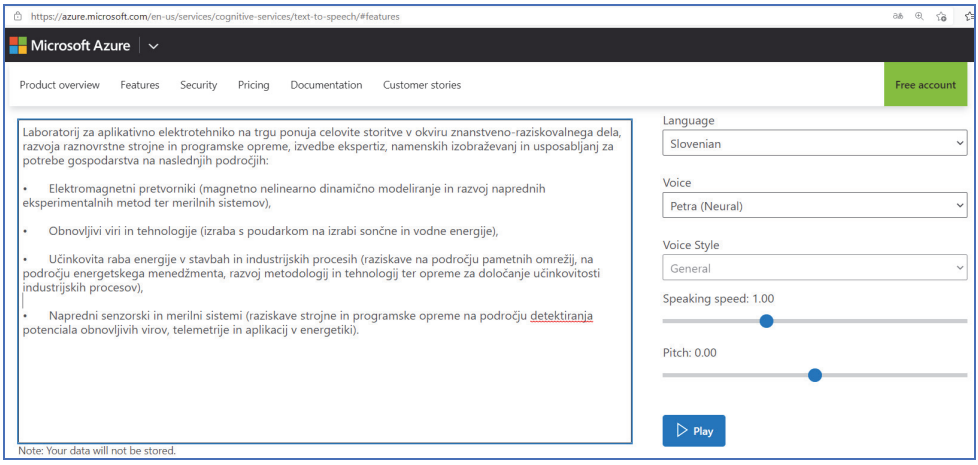

Figure 3: *Example of using MS Azure*

There are three options to choose from in Azure Voice options: Petra and Rok (both are Neural voices) and the voice Lado from the basic MS office option. Next to settings of the Speaking speed, it is also possible to adjust the Pitch of the chosen voice (Figure 3).

The Microsoft Azure - Text to Speech demo app gives the best loud reading results of the Slovenian language but does not allow saving speech as a recording directly. To solve this, the Windows 10 Game Bar was activated, and a video of the screen was recorded during the Text to Speech. The recorded mpeg4 file was then converted to an mp3 file with the VLC player.

4.4 Publishing a Virtual Tour

At the end of the editing process, the Virtual Tour needs to be published to a web server to share users easily via the Internet. Using the 3dVista hosting service is the easiest way to get your Virtual Tour online. This is an optional service to upload a Virtual Tour fast and easily, a service which is paid for annually for the hosting space you contract.

Another option is to upload a Virtual Tour to a server other than the 3dVista hosting service, in which case an FTP client is needed. An FTP client is a program that helps transfer files like the

Virtual Tour file, between the computer and the external server where the domain is located. An FTP client called FileZilla was used, because it is free and easy to use.

4 CONCLUSIONS

Because of COVID-19, there were a lot of restrictions on public gatherings, and therefore it was not possible to perform a lot of typical events, such as information day of Faculties and other laboratory presentations.

A variety of industries use the Virtual Tour technology to help promote their services and products. For most business purposes, a Virtual Tour must be accessible from everywhere, therefore, a major solution is a web-based Virtual Tour. Over the last few years the quality and accessibility of Virtual Tours has improved considerably, with some websites allowing the user to navigate the tours by clicking on maps or integrated floor plans. The main areas where this new technology is applied is mainly universities, the Tourism and Culture sectors and the Real-estate industry.

With the help of a 360° camera, 3dVista software and existing material (pdf text, photos, and videos), a Virtual Tour was created of the Institute of Energy Technology located in Krško. Within this Virtual Tour, a user can move between laboratories, inspect laboratory equipment, read technical specifications, watch embedded movies about the Faculty, and even listen to text-to-speech descriptions of laboratories.

With the help of the Virtual Tour of the laboratories, a virtual conference with a virtual walkthrough of the laboratories was performed with great success. The moderator was able to present all the rooms, and the Professors could describe the equipment available and the field of work of every laboratory.

Figure 4: *Snapshot fromthe Virtual Tour*

References

[1] **N.L. Yeo, M.P.White, I.Alcock, R.Garside, S.G.Dean, A.J.Smalley, B.Gatersleben**: *What is the best way of delivering virtual nature for improving mood? An experimental comparison of high-definition TV, 360◦ video, and computer generated virtual reality*, Journal of Environmental Psychology, 72, 2020

[2] **A.Osmani, N.A.Wahab, M.H.Ismail:** *Development and Evaluation of an Interactive 360° Virtual Tour for Tourist Destinations,* Journal of Information Technology Impact, Vol. 9, No. 3, pp. 173-182, 2009

[3] **L.Argyriou, D.Economou, V.Bouki:** *Design methodology for 360° immersive video applications: The case study of a cultural heritage virtual tour***,** Personal and Ubiquitous Computing, Vol:24, pp.843–859, 2020

[4] **A.S.Pahlevi, J.Sayono, Y.A.L.Hermanto**: *Design of a Virtual Tour as a Solution for Promoting the Tourism Sector in the Pandemic Period*, ICADECS, 2021

[5] **A.A. Pilarska, P. Tomczykowska:** *Virtual tourism space of cities,* Journal of Modern Science, Vol.38, pp. 317-333, 2018

[6] **M.Colasante:** *Nicola Building Virtual Tour; Considering simulation in the equity of experience concept*, ASCILITE, 2011

[7] **HM.Chiao, YL.Chen, WH.Huang:** *Examining the usability of an online virtual tour-guiding platform for cultural tourism education,* Journal of Hospitality, Leisure, Sport & Tourism Education, Vol.23, pp.29-38, 2018

[8] **THETA:** *RICOH THETA Z1 camera specifications*, https://support.theta360.com/

[9] **3DVISTA ESPAÑA S.L.:** *3DVista Virtual Tour Suite*, 01/08/2014

http://download.3dvista.com/current/vts/3DVistaVT-QuickGuide.pdf

[10] **3DVista:** *Tutorial: Text To Speech - Automatic Narration of Texts inside Virtual Tours* https://www.youtube.com/watch?v=-nO6GDUABfw

[11] **Azure:** *Text to Speech - A Speech service feature that converts text to lifelike speech*, https://azure.microsoft.com/en-us/services/cognitive-services/text-to-speech/#overview

Journal of Energy Technology

JET Volume 14 (2021) p.p. 69-78
Issue 4, December 2021
Type of article 1.01
www.fe.um.si/en/jet.html

FROST PROTECTION MEASURES: SURVEY RESULTS

ZAŠČITNI UKREPI PROTI POZEBI: REZULTATI ANKETE

Matej Fike[✉], Miha Smrekar[1], Mateja Fekonja[2]

Keywords: Spring Frost, Active Frost Protection, Passive Frost Protection, Survey Results

Abstract

In Slovenia, frosts occur often and it causes great damage for growers. Various passive and active methods are known for frost protection. Pasive methods can be implemented throughout the year. They are used to enable easier implementation of active methods, which are in use when a period of frost occurs. The aim of this research is, with the help of a survey, to assess whether growers in Slovenia implement active or passive methods of frost protection, and if not, why not. The survey contained 24 questions and was intended primarily for fruit and wine growers in Slovenia. The results of the survey show that frost happens to Slovenian growers on average every other year, and destroys on average 50% of their crop. Despite frequent frosts and the damage they cause, growers are not implementing any active measures, nor are they willing to invest in them. The reasons for this may be the large investments required for active measures, the small sizes of farms in Slovenia (on average 12 ha according to the survey answers), or that farmers are insufficiently informed about the various measures.

[✉] Corresponding author: Doc. Dr, Matej Fike, Faculty of Energy Technology, Hočevarjev trg 1, SI-8270 Krško, Tel.: +386 7 6202 228, E-mail address: matej.fike@um.si,

[1] Faculty of Energy Technology, Hočevarjev trg 1, 8270 Krško

[2] Faculty of Agriculture and Life Sciences, Pivola 10, 2311 Hoče

Povzetek

V Sloveniji je pogostost pozeb zelo velika, kar pridelovalcem povzroča veliko škode. Za zaščito proti pozebi poznamo različne pasivne in aktivne metode. Pasivne metode lahko izvajamo skozi vso leto, z njimi pa omogočimo lažje izvajanje aktivnih metod, ki jih uporabimo, ko nastopi obdobje pozeb. Cilj te raziskave je bil s pomočjo ankete oceniti, v kolikšni meri pridelovalci v Sloveniji izvajajo aktivne oziroma pasivne ukrepe za zaščito pred pozebo in če jih ne, zakaj ne. Anketa je vsebovala 24 vprašanj in je bila namenjena predvsem sadjarjem in vinogradnikom v Sloveniji. Rezultati ankete kažejo, da slovenski pridelovalci utrpijo škodo zaradi pozebe v povprečju vsako drugo leto, ta pa jim uniči 50 % pridelka. Kljub pogostim pozebam in veliki škodi, ki jo le-te povzročijo, pa se pridelovalci za različne aktivne ukrepe ne odločajo, niti niso pripravljeni v njih investirati. Razlog za to je lahko v visokih investicijah, ki so potrebne za aktivne ukrepe, majhnosti kmetij v Sloveniji (povprečno 12 ha glede na odgovore ankete) ali pa v tem, da so kmetje o različnih ukrepih premalo informirani.

1 INTRODUCTION

As a consequence of climate changes, an increased variability has been recorded in the frequency and timing of frost events. Such events have a strong impact on agriculture, as cold temperatures affect plant survival. Higher average temperatures in spring mean earlier phenological development of plants, and, thus, an increased risk of frost damage when sudden low temperatures occur [1].

In Slovenia, frosts occur often, and it causes great damage for growers. Since 1987, it has been observed that spring phenological phases appear earlier, due to higher air temperatures, which means that plants bloom faster, and, thus, increase the risk of spring frost. Every decade the air temperature rises slightly, and because of this, fruit trees bloom earlier, e.g. apples 2 days earlier, pears 4 to 5 days earlier and cherries 3 days earlier per ten years. Frost not only causes damage due to crop loss, but we must also account for economic costs due to small fruits with shorter storage time, the costs of various measures to preserve the fruits left after the frost, as well as the costs of measures to take care of the affected plants in the following years [2].

Frost inflicts damage to plant tissues caused by low temperatures. If the cell juice freezes in the plant, it causes mechanical damage to cell organs and cell destruction [3]. For most fruit plants, the freezing of flowers is caused by temperatures below -2 ° [4]. The damage caused by the frost depends mainly on the fruit species or variety, and on the development phase of the plant [5]. Depending on the time of the occurrence, we divide frost into autumn, winter and spring frosts. Late spring frosts do the most damage. There are also several types of frost, namely radiation, advection, combined and evaporative frost [6].

Plantations can be protected from frost by active or passive methods. Passive methods are usually cheaper, and are used before the onset of frost. However, they cannot protect the plantation completely from frost, but, because they are quite effective against advection frost, they can be combined with active methods. Active methods are used during the onset of frost, and are usually much more expensive due to the maintenance and manual labour costs [7].

The aim of this research is, with the help of a survey, to assess whether growers in Slovenia have implemented active or passive methods of frost protection, and, if not, why not. The survey contained 24 questions and was intended primarily for fruit and winegrowers in Slovenia.

2 DATA AND METHODS

2.1 Passive frost protection methods

Passive protection includes methods that are implemented before frost events to help avoid the need for active protection. Passive methods are usually less costly than active methods, and are often beneficial to eliminate the need for active protection [8].

Possible passive measures for new plantations are location selection, which includes taking into account the location temperatures during the frost season, removal of cold air from the plantation, if cold air can be guided out of the orchard, tree architecture – trimming and cultivating trees in an appropriate manner to reduce damage by the radiative hoarfrost, and an appropriate selection of fruit species, varieties and rootstocks. For each fruit species, breeders can select and cross more resistant varieties that are less susceptible to frost, drought, diseases and pests. Possible passive measures for existing plantations include timely and correct cutting of plants, hail nets and other protective foils and textiles, fruit plants, tree trunk bleaching, and soil care and irrigation [3].

2.2 Active frost protection methods

Active protection measures are implemented during a frosting event to mitigate the effects of sub-zero temperatures. The cost varies, depending on local availability and prices [8].

Heaters provide protection against frosting events by direct radiation to the plants and by causing convective mixing of air within the inversion layer. They are reported to be less efficient when there is no inversion layer [9]. The energy requirement to match plant heat losses during a radiation frost night is in the range of 10-50 W/m^2, and the common heater energy output range is 140-280 W/m^2. Because the energy output is greater than the energy losses, much of the energy output from the heaters is lost, and modern heaters have little control over the temperature of the gases emitted [8].

Wind machines are used to prevent or mitigate the adverse effects of frost events in spring, and they reduce the plant heat losses by eroding the thermal inversion, and warm air is blown downward from aloft into the cold canopy. In [10], for example, they record an effective temperature increase area of 3-5 ha around the wind machine.

Sprinkler irrigation has been applied for frost protection in orchards, and has achieved good frost protection effects. The protection is based on a method of reducing the heat losses from the plants by increasing the temperature of the leaves above a certain temperature. In this way, a lower portion of heat is lost (around 83.7 kJ/kg), as opposed to the phase change that occurs at the freezing temperatures of water (around 334.5 kJ/kg) [11]. The energy consumption of sprinklers is lower than that of heaters, so the variable costs are low. The disadvantages are the high installation costs and the large amount of water needed [8].

Helicopters move warm air from aloft in a temperature inversion to the colder surface. The area covered by a single helicopter depends on the helicopter`s size and weight and the weather conditions. The estimated coverage area by a single helicopter varies between 22 and 44 ha [12].

2.3 Survey

As part of the Student Innovative Project for Social Benefit (ŠIPK) we conducted a survey, and thus obtained information on the impact of frost on local agriculture. The survey was conducted in electronic form with the help of the online provider 1 ka.

The survey included 24 questions on the topic of frost and frost protection measures. The target respondents were agricultural landowners, especially fruit growers, winegrowers and berry growers. Data collection took place from 10. 6. 2020 to 25. 6. 2020. A total of 35 respondents completed the survey at least in part.

In the survey we wanted to get the followinginformation :

a) The frequency of frost among growers,
b) The damage caused by frost,
c) The frost prediction accuracy,
d) The use of active/passive methods,
e) The reasons for not using protection,
f) Willingness to invest in frost protection.

3 RESULTS

35 surveys were conducted with farmers who are engaged mainly in fruit growing or viticulture. The majority (39%) of respondents have a size of production areas from 0-6 ha, followed by farms of 7-12 ha (24%), 13-18 ha (15%), and then the remaining farms larger than 19 ha (21%). On average, these are small to medium-sized plantations (Figure 1).

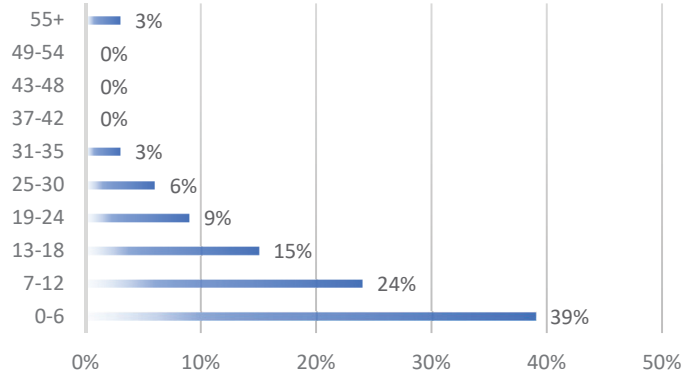

Figure 1: *What is the total size of your cultivable land (ha)? (n=33)*

Most of the agricultural plantations of the respondents lie at altitudes of 171 to 425 meters (Figure 2).

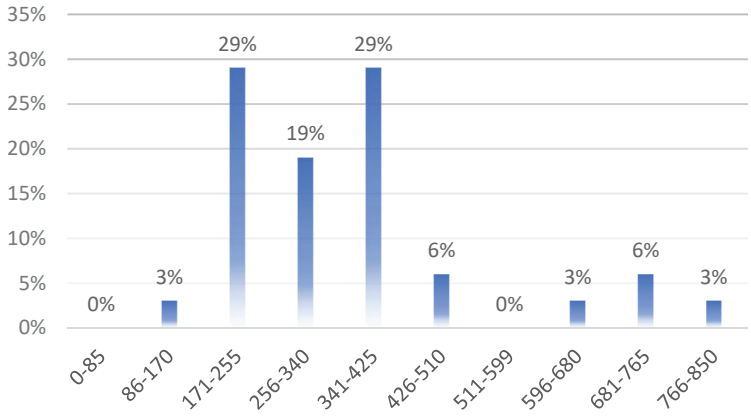

Figure 2: *What is the average altitude of your cultivable land (m)? (n=31)*

The survey data show that on the farms of the respondents frost occurs on average twice a year (48%), 39% of frost occurs once a year, and a small proportion also have frost five or six times a year. Altogether, this means that 87% of respondents experience frost at least once a year (Figure 3).

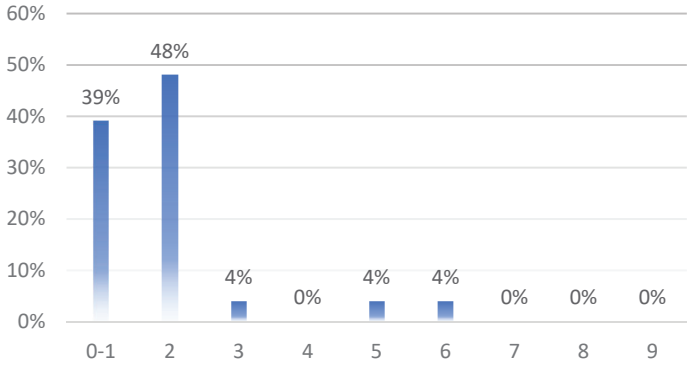

Figure 3: *How many times a year does frost occur on average on your farm? (n=23)*

Based on the answers to the survey, it is evident that, in Slovenia, respondents experience frost in a plantation 4.5 times in 10 years, which means that frost occurs on average approximately every other year (Figure 4).

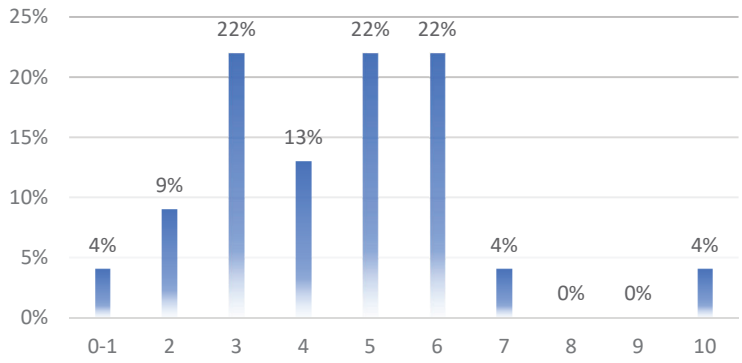

Figure 4: *How many frosty years have you had in the last ten years? (n=23)*

The survey shows that, on average, for respondents, the frost destroys a little more than half of the crop (50.7%) (Figure 5).

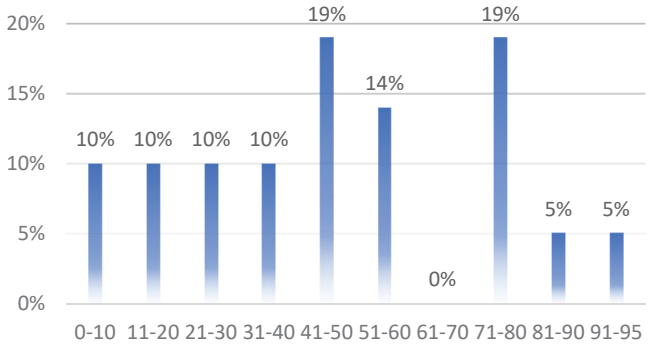

Figure 5: *On average, what percentage of your crop was destroyed by frost [%]? (n=21)*

Most respondents are moderately satisfied with the frost forecasts. Growers mostly use forecasts available on the Internet and on television, and rarely use the meteorological portal of the Slovenian Environment Agency. The vast majority of growers do not use other methods to obtain weather data (Figure 6).

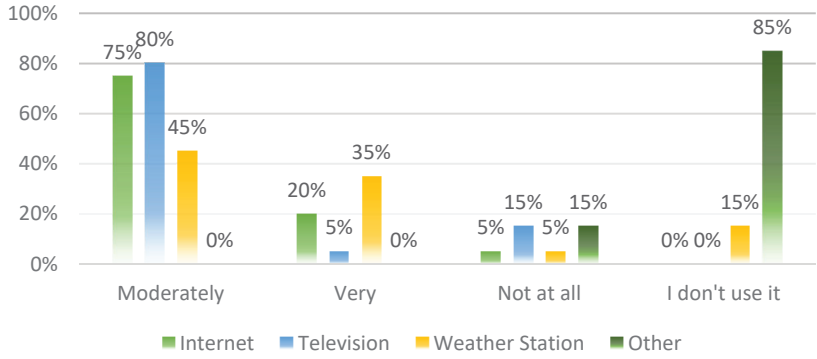

Figure 6: *How satisfied are you with frost forecasts? Are the predictions accurate? (n=25)*

The analysis shows that growers use preventive measures, especially choosing fruit species that are less sensitive to frost (50% of respondents). Among other commonly used measures, growers listed valerian spraying and biostimulators (29%). 25% of them use protective foils or textiles, 17% of them preventively bleach trunks. Only 13% of respondents plan new plantations on the shady side, where the possibility of frost is lower, and only 13% make proper nutrition plans. Only 8% of respondents started directing the air past the plantation.

Most respondents are well aware of active measures against frost, but only 10% of them use smoking, 5% use classical sprinkling and 5% paraffin candles, and, altogether, 80% of the respondents do not use any active measure to protect against spring frost.

In the next question, the respondents answered that active measures are too expensive for them (76%), or that they think they are ineffective, or they do not know about them (24%). Passive measures are too expensive for 55% of respondents, 30 % do not know them well enough, and 15% consider them ineffective (Figure 7).

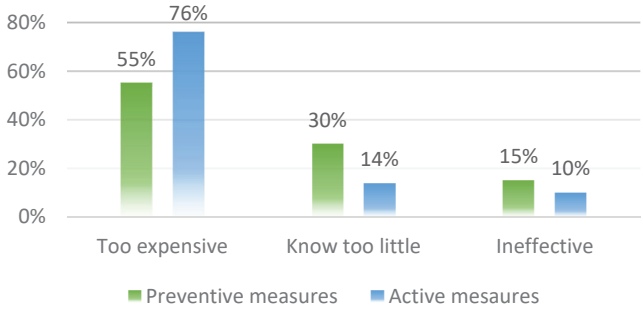

Figure 7: *In case you decided not to use preventive/active measures, why not? (n=21)*

When asked how much they would be willing to invest for frost protection that would be effective, most answered that they are willing to invest less than €500 per ha (59%), and a good third would be willing to invest up to €1000 per ha (Figure 8).

Also, respondents are not prepared to invest more than €500 per ha per year for the operation or maintenance of a frost protection system (Figure 9).

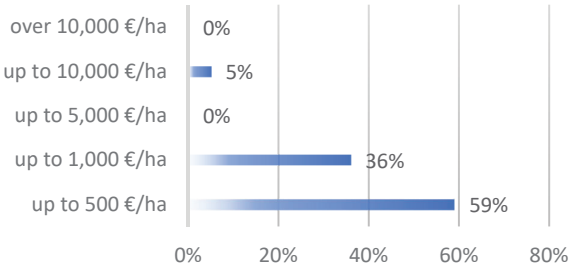

Figure 8: *How much would you be prepared to invest in frost protection that would be effective? (n=22)*

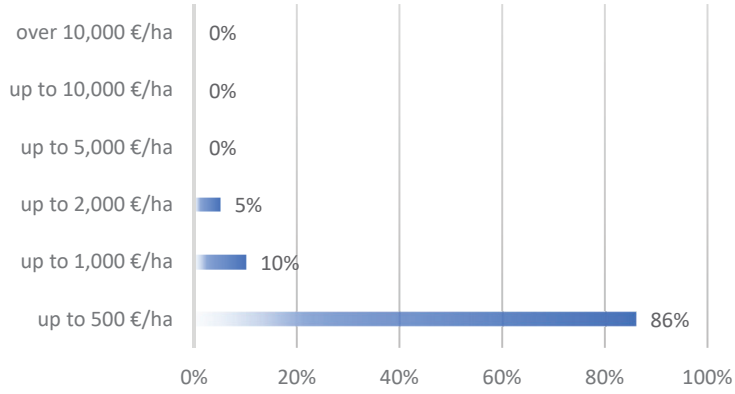

Figure 9: *How much money are you prepared to pay annually for the maintenance or operation of such a system? (n=21)*

4 CONCLUSION

Based on the survey data from 35 farms, ranging from 1 to 55 hectares, we concluded that 87% of the surveyed fruit growers are affected by frost every season, many twice or more per year. On average, 50.2% of fruit is destroyed during frosting events. Only 50% of farms use passive frost protection measures, and only 5-10% are using active frost protection measures. Despite this, only 12% of them are looking into the possibilities of investing in frost protection systems. When asked how much they were willing to invest in frost protection, 59% of the respondents are willing to invest in an efficient system up to €500 per ha. When asked why they do not opt for active/passive measures, most of them answered that they are too expensive for them. In conclusion, farm owners would more likely implement active and passive measures if the acquisition costs or operation costs of the protection methods were lower. One possible solution is to use passive protection measures, which can be beneficial in reducing the frost damage to plants, while being considerably cheaper than active protection measures. Also, when deciding on investing in an active system, farmers should make a long-term economic analysis to evaluate the potential economic benefit of the installed protection measures.

5 REFERENCES

[1] M. Hadad, . J. C. Tardif, F. Conciatori, . J. Waito and A. Westwood, "Climate and atmospheric circulation related to frost-ring formation in Picea mariana trees from the Boreal Plains, interior North America," *Weather and Climate Extremes,* vol. 29, 2020.

[2] Agencija Republike Slovenije za okolje, "Mesečni bilten Republike Slovenije za okolje," *Naše okolje,* vol. 4, pp. 53-60, 2017.

[3] EIP-AGRI, "Zaščita pridelka sadja pred pozebo," 2019.

[4] A. Žust, "Spomladanska pozeba v Primorju 8. aprila 2003," *UJMA,* vol. 17/18 (2003/2004), pp. 135-138, 2003.

[5] I. Kodrič, M. Lukačič and J. Prošek, Zaščita pred spomladansko pozebo, Ljubljana: Ministry of Agriculture, Forestry and Food of Slovenia, 2006.

[6] A. Žust and A. Sušnik, "Spomladanska pozeba," *UJMA,* vol. 10, pp. 59-63, 1996.

[7] I. Zhou, J. Lipman, M. Abolhasan, N. Shariati and D. W. Lamb, "Frost Monitoring Cyber–Physical System: A Survey on Prediction and Active Protection Methods," *IEEE Internet of Things Journal,* vol. 7, 2020.

[8] R. Snyder, P. d. M.-A. J. and S. Matulich, Frost Protection: fundamentals, practice and economics, Rome: Food and Agriculture Organization of the United Nations, 2005.

[9] R. Snyder, "Principles of Frost Protection," University of California, Davis, 2000.

[10] V. Heusinkveld, A. Hooft, B. Schilperoort, P. Baas, M. Veldhuis and B. Wiel, "Towards a physics-based understanding of fruit frost protection using wind machines," *Agricultural and Forest Meteorology,* Vols. 282-283, no. 107868, 2020.

[11] H. Yongguang, C. Z., L. Pengfei, A. Amoah and L. Pingping, "Sprinkler irrigation system for tea frosting protection and the application effect," *International Journal of Agricultural and Biological Engineering,* vol. 9, no. 5, pp. 17-23, 2016.

[12] A. Soršak, Z. Gutman-Kobal, I. Kodrič and D. Koron, Tehnološka navodila za zaščito pred spomladansko pozebo, 2018.

Nomenclature

(Symbols)	(Symbol meaning)
ŠIPK	Študentski inovativni projekti za družbeno korist (Student innovative projects for social benefit)
n	Number of respondents

Journal of Energy Technology

Author instructions

www.fe.um.si/en/jet.html

MAIN TITLE OF THE PAPER
SLOVENIAN TITLE

*Author[1], Author [2], Corresponding author*ℜ

Keywords: (Up to 10 keywords)

Abstract

Abstract should be up to 500 words long, with no pictures, photos, equations, tables, only text.

Povzetek

(Abstract in Slovenian language)

Submission of Manuscripts: All manuscripts must be submitted in English by e-mail to the editorial office at jet@um.si to ensure fast processing. Instructions for authors are also available online at http://www.fe.um.si/en/jet/author-instructions.html.

Preparation of manuscripts: Manuscripts must be typed in English in prescribed journal form (MS Word editor). A MS Word template is available at the Journal Home page.

A title page consists of the main title in the English and Slovenian language; the author(s) name(s) as well as the address, affiliation, E-mail address, telephone and fax numbers of author(s). Corresponding author must be indicated.

Main title: should be centred and written with capital letters (ARIAL bold 18 pt), in first paragraph in English language, in second paragraph in Slovenian language.

Key words: A list of 3 up to 6 key words is essential for indexing purposes. (CALIBRI 10pt)

Abstract: Abstract should be up to 500 words long, with no pictures, photos, equations, tables, - text only.

Povzetek: - Abstract in Slovenian language.

Main text should be structured logically in chapters, sections and sub-sections. Type of letters is Calibri, 10pt, full justified.

ℜ Corresponding author: Title, Name and Surname, Organisation, Department, Address, Tel.: +XXX x xxx xxx, E-mail address: x.x@xxx.xx

[1] Organisation, Department, Address

[2] Organisation, Department, Address

Units and abbreviations: Required are SI units. Abbreviations must be given in text when first mentioned.

Proofreading: The proof will be send by e-mail to the corresponding author in MS Word's Track changes function. Corresponding author is required to make their proof corrections with accepting or rejecting the tracked changes in document and answer all open comments of proof reader. The corresponding author is responsible to introduce corrections of data in the paper. The Editors are not responsible for damage or loss of submitted text. Contributors are advised to keep copies of their texts, illustrations and all other materials.

The statements, opinions and data contained in this publication are solely those of the individual authors and not of the publisher and the Editors. Neither the publisher nor the Editors can accept any legal responsibility for errors that could appear during the process.

Copyright: Submissions of a publication article implies transfer of the copyright from the author(s) to the publisher upon acceptance of the paper. Accepted papers become the permanent property of "Journal of Energy Technology". All articles published in this journal are protected by copyright, which covers the exclusive rights to reproduce and distribute the article as well as all translation rights. No material can be published without written permission of the publisher.

Chapter examples:

1 MAIN CHAPTER

(Arial bold, 12pt, after paragraph 6pt space)

1.1 Section

(Arial bold, 11pt, after paragraph 6pt space)

1.1.1 Sub-section

(Arial bold, 10pt, after paragraph 6pt space)

Example of Equation (lined 2 cm from left margin, equation number in normal brackets (section. equation number), lined right margin, paragraph space 6pt before in after line):

Equation (1.1)

Tables should have a legend that includes the title of the table at the top of the table. Each table should be cited in the text.

Table legend example:

Table 1: *Name of the table (centred, on top of the table)*

Figures and images should be labelled sequentially numbered (Arabic numbers) and cited in the text – Fig.1 or Figure 1. The legend should be below the image, picture, photo or drawing.

Figure legend example:

Figure 1: *Name of the figure (centred, on bottom of figure, photo, or drawing)*

References

[1] **N. Surname:** *Title,* Journal Title, Vol., Iss., p.p., Year of Publication

[2] **N. Surname:** *Title,* Publisher, Year of Publication

[3] **N. Surname:** *Title* [online], Publisher or Journal Title, Vol., Iss., p.p., Year of Publication. Available: website (date accessed)

Examples:

[1] **J. Usenik**: *Mathematical model of the power supply system control*, Journal of Energy Technology, Vol. 2, Iss. 3, p.p. 29 – 46, 2009

[2] **J. J. DiStefano, A.R. Stubberud, I. J. Williams**: *Theory and Problems of Feedback and Control Systems*, McGraw-Hill Book Company, 1987

[3] **T. Žagar, L. Kegel:** *Preparation of National programme for SF and RW management taking into account the possible future evolution of ERDO* [online], Journal of Energy Technology, Vol. 9, Iss. 1, p.p. 39 – 50, 2016. Available: http://www.fe.um.si/images/jet /Volume 9_Issue1/03-JET_marec_2016-PREPARATION_OF_NATIONAL.pdf (7. 10. 2016)

Example of reference-1 citation: In text *[1],* text continue.

Nomenclature

(Symbols)	(Symbol meaning)
t	time

JET

JET I Journal of Energy Technology I Vol. 14, Issue 4, December 2021 I University of Maribor, Faculty of Energy Technology

ISSN 1855-5748

9 771855 574008